



HAL
open science

Mantle xenolith-bearing phonolites and basanites feed the active volcanic ridge of Mayotte (Comoros archipelago, SW Indian Ocean)

Carole Berthod, Etienne Médard, Andrea Di Muro, Théo Hassen Ali, Lucia Gurioli, Catherine Chauvel, Jean-Christophe Komorowski, Patrick Bachèlery, Aline Peltier, Mhammed Benbakkar, et al.

► To cite this version:

Carole Berthod, Etienne Médard, Andrea Di Muro, Théo Hassen Ali, Lucia Gurioli, et al.. Mantle xenolith-bearing phonolites and basanites feed the active volcanic ridge of Mayotte (Comoros archipelago, SW Indian Ocean). *Contributions to Mineralogy and Petrology*, 2021, 176 (10), pp.75. <10.1007/s00410-021-01833-1>. <hal-03442154>

HAL Id: hal-03442154

<https://hal.science/hal-03442154v1>

Submitted on 23 Nov 2021

HAL is a multi-disciplinary open access archive for the deposit and dissemination of scientific research documents, whether they are published or not. The documents may come from teaching and research institutions in France or abroad, or from public or private research centers.

L'archive ouverte pluridisciplinaire **HAL**, est destinée au dépôt et à la diffusion de documents scientifiques de niveau recherche, publiés ou non, émanant des établissements d'enseignement et de recherche français ou étrangers, des laboratoires publics ou privés.



HAL Authorization

[Click here to view linked References](#)

1 Mantle xenolith-bearing phonolites and basanites feed the active 2 volcanic ridge of Mayotte (Comoros archipelago, SW Indian 3 Ocean)

4
5 Carole Berthod⁽¹⁾, Etienne Médard⁽¹⁾, Andrea Di Muro^(2,3), Théo Hassen Ali⁽¹⁾, Lucia
6 Gurioli⁽¹⁾, Catherine Chauvel⁽³⁾, Jean-Christophe Komorowski⁽³⁾, Patrick Bachèlery⁽¹⁾, Aline
7 Peltier^(2,3), Mhammed Benbakkar⁽¹⁾, Jean-Luc Devidal⁽¹⁾, Pascale Besson⁽³⁾, Anne Le Friant⁽³⁾,
8 Christine Deplus⁽³⁾, Sophie Nowak⁽³⁾, Isabelle Thinon⁽⁴⁾, Pierre Burckel⁽³⁾, Samia Hidalgo⁽³⁾,
9 Nathalie Feuillet⁽³⁾, Stephan Jorry⁽⁵⁾, Yves Fouquet⁽⁵⁾.

10
11
12 (1) Université Clermont Auvergne, CNRS, IRD, OPGC, Laboratoire Magmas et Volcans,
13 Clermont-Ferrand, France,

14 (2) Observatoire Volcanologique du Piton de la Fournaise, Institut de physique du globe de
15 Paris, F-97418 La Plaine des Cafres, France

16 (3) Université de Paris, Institut de physique du globe de Paris, CNRS, F-75005 Paris, France

17 (4) BRGM, French Geological Survey, 3 avenue Claude Guillemin, BP36009, 45 060
18 Orléans, Cédex 2, France,

19 (5) Ifremer, Unité Géosciences Marines, F-29280 Plouzané, France

20
21 **Keywords:** Mayotte; Basanite; phonolite; magmatic system; fractional crystallization.

22 23 **Abstract**

24 Since 2018, the submarine east flank of Mayotte Island (Comoros archipelago) is the
25 site of a major and still ongoing eruption, located at 3.5 km depth bsl on a WNW-ESE
26 volcanic ridge. Oceanographic cruises carried out to monitor this seismo-volcanic crisis
27 allowed us to determine that this volcanic ridge is built by a bimodal sodic alkaline magmatic
28 series that includes basanites and phonolites. A petrological study of dredged samples allowed
29 us to image the magmatic system feeding the volcanic ridge and to determine the link
30 between basanitic and phonolitic magmas. The magmatic system feeding the volcanic ridge
31 comprises multiple levels of magma storage. Basanitic magmas generated at 80-100 km
32 mantle depth are stored in one or more deep reservoir(s) (≥ 37 km) and then in shallower

33 basanitic and phonolitic lenses located close to the Moho interface before rising the surface.
34 This study identifies three possible scenarios: (1) the deep basanitic magma rises directly and
35 quickly to the surface from the deep mantle reservoir (as is currently happening 60 km
36 offshore), (2) the basanitic magma stalls in a shallower reservoir near the Moho before
37 resuming its ascent toward the surface and erupting as porphyritic basanite, (3) the basanitic
38 magma stops and evolves to phonolite in these sub-crustal reservoirs. The phonolitic lavas are
39 produced by approximately 80% fractional crystallization (34% clinopyroxene, 30%
40 anorthoclase feldspar, 15.5% magnetite, 12.5% olivine, 5% apatite and 4% ilmenite) of a
41 hydrous basanitic magma at mantle depths ($P > 0.6$ GPa) under reduced oxygen fugacity
42 (\sim FMQ-1). In this third scenario, the phonolitic magma might be reactivated by the arrival of
43 a new batch of deeper basanitic magma.

44 45 **1. Introduction**

46
47 The deepest part (3.5 km bsl) of the eastern submarine flank of Mayotte is the site of a
48 long lasting and still ongoing (as of January 2021) effusive volcanic activity that followed an
49 intense volcano-tectonic crisis beginning in May 2018 (Berthod et al., 2021; Cesca et al.,
50 2020; Feuillet et al., 2021; Lemoine et al., 2020). A series of oceanographic cruises organized
51 by the French scientific community have led to the discovery of an active volcanic ridge
52 characterized by basanitic and phonolitic volcanic cones and lava fields, and extending along
53 60 km from the deep distal eruptive site to the subaerial easternmost part of Mayotte island,
54 Petite Terre (Feuillet, 2019; Feuillet et al., 2021; Fouquet and Feuillet, 2019; Jorry, 2019).
55 Both subaerial and submarine phonolitic eruptive products carry mm to dm sized ultramafic
56 xenoliths testifying to rapid ascent from mantle levels. Worldwide, most phonolitic magmas
57 evolve and reside in shallow crustal reservoirs (e.g., Scaillet et al. 2008; Grant et al. 2013;
58 Moussallam et al. 2013), and mantle xenolith-bearing phonolites are extremely rare (Dautria
59 et al., 1983; Grant et al., 2013; Price and Green, 1972). Phonolites usually result from
60 fractional crystallization of a basanitic parental magma (Ablay et al., 1998; Kyle et al., 1992;
61 Le roex et al., 1990), although phonolitic melts can be generated directly by mantle melting
62 (Laporte et al., 2014). Berthod et al. (2021) demonstrate that lavas erupted in 2018-2019 from
63 the distal submarine site are basanitic and ascended rapidly from a large deep reservoir
64 located in the lithospheric mantle. Slight chemical evolution of the erupted lavas over time
65 was interpreted as an evidence of syn-eruptive mixing between the ascending basanite and a
66 shallower, cooler and more differentiated magma possibly stored close to the Moho interface.

67 Long-standing activity on the Mayotte active volcanic ridge allows us to explore the origin of
68 deep phonolites and their evolution at mantle level together with their link with the basanite
69 volcanism. Are basanite and phonolites both primitive mantle melting products? Or do
70 phonolites derive through fractional crystallization of the basanites?

71
72 In order to answer these questions, we performed a detailed petrological and geochemical
73 investigation, including petrological analysis, thermobarometry and in situ and whole-rock
74 geochemistry of the submarine volcanic products collected along the Mayotte submarine
75 ridge during three successive oceanographic cruises (MAYOBS 1, MAYOBS 2 and
76 MAYOBS 4) between May and July 2019 (Feuillet, 2019; Feuillet et al., 2019; Fouquet and
77 Feuillet, 2019; Jorry, 2019), and compared them with recent (Holocene) subaerial products
78 collected during two field campaigns on Petite Terre in 2018 and 2019.

79 80 **2. Geological setting**

81
82 The Comoros Archipelago, located in the Mozambique Channel between the northern tip
83 of Madagascar and the eastern coast of Mozambique (Fig. 1a) consists of four islands:
84 Mayotte, Anjouan, Moheli and Grande Comore, from east to west. These islands are
85 interconnected by a series of submarine volcanic ridges and are associated with atolls and
86 partially emerged reef platforms (Tzevahirtzian et al. 2021). The overall archipelago has been
87 recently interpreted as the NE-SW boundary between the Lwandle microplate and the
88 Somalia plate, a boundary marked by a zone of active seismicity connecting the northern
89 extremity of Madagascar in the east to the African coast in the west (Bertil and Regnault,
90 1998; Dziewonski et al., 1981; Ekström et al., 2012; Famin et al., 2020). This boundary may
91 consist in a zone of broad deformation extending up to the northern half of Madagascar
92 (Stamps et al., 2021) or in a more localized dextral transfer zone between the offshore branch
93 of the East-African rift and Madagascar (Famin et al., 2020; Feuillet et al., 2021).

94 The origin of Comorian volcanism is a long-lasting debate (Bachèlery and Hémond, 2016;
95 Class et al., 2009; Claude-Ivanaj et al., 1998; Coltorti et al., 1999; Deniel, 1998a; Flower,
96 1973; Michon, 2016; Nougier et al., 1986; Pelleter et al., 2014; Strong, 1972; Thompson and
97 Flower, 1971; Tzevahirtzian et al., 2021). According to the latest investigations, it is likely
98 associated with lithospheric deformation possibly in relation with the East African Rift
99 System (Courgeon et al., 2017; Lemoine et al., 2020; Michon, 2016; Nougier et al., 1986;
100 Tzevahirtzian et al., 2021), rather than being the result of the interaction of a mantle plume

101 with oceanic lithosphere (Class et al., 2009, 2005, 1998; Class and Goldstein, 1997; Claude-
102 Ivanaj et al., 1998; Deniel, 1998b; Emerick and Duncan, 1982; Hajash and Armstrong, 1972).

103 Mayotte, the easternmost part of the archipelago, is composed of a main volcanic island
104 (Grande Terre) and a volcanic islet (Petite Terre), located 4 km east of Grande Terre and built
105 on the modern barrier reef (Nehlig et al., 2013). Mayotte subaerial activity is subdivided into
106 multiple phases of volcanism beginning in the southern part of Grande Terre (10.6 – 1.9 Ma)
107 and then migrating toward the north (5 – 0.75 Ma) and the northeast (0.75 – Present)
108 separated by periods of quiescence (Debeuf, 2004; Pelleter et al., 2014). Magmas emitted on
109 Mayotte show a wider range of differentiation compared to the other islands of the Comoros
110 archipelago, and they define two magmatic series ranging from strongly silica-undersaturated
111 alkaline magmas in the older series to weakly alkaline magmas in the most recent ones (Fig.
112 2a).

113 Mayotte is considered the oldest island of Comoros archipelago with a maximum age of
114 20 Ma for the submarine onset of magmatic activity (Debeuf, 2004; Emerick and Duncan,
115 1982; Hajash and Armstrong, 1972; Michon, 2016; Nougier et al., 1986; Pelleter et al., 2014;
116 Tzevahirtzian et al., 2021). Despite being the oldest island of the archipelago, Holocene
117 volcanic activity has been documented both on land (Zinke et al., 2003) and on its submarine
118 flanks. In May 2018, an intense seismo-volcanic crisis began on the distal part of a 60 km
119 long NW-SE volcanic ridge that runs off the eastern submarine flank of Mayotte (Fig. 1b;
120 Cesca et al. 2020; Lemoine et al. 2020). This WNW-ESE-oriented volcanic ridge extends
121 from the site of the ongoing eruption in the east to Petite Terre Island in the west (Berthod et
122 al., 2021; Feuillet et al., 2021), see Figure 1). Petite Terre is indeed characterized by the
123 presence of very recent (200 to 4 ka; Zinke, (2003)) phonolitic phreatomagmatic activity with
124 well-preserved maar structures, and strombolian mafic cones aligned on N140 fractures.
125 Strombolian mafic cones are also present in the lagoon between Grande Terre and Petite
126 Terre.

127 The presence of these recent volcanic structures along the east coast of Mayotte and the
128 ongoing submarine eruption on the east flank of the island raises the question of the possible
129 triggering of a future volcanic activity on the island itself. Indeed, ongoing volcanic
130 seismicity is not only present below the active volcano, 60 km from the island, but the most
131 significant seismic activity is currently recorded 5 – 15 km offshore the island of Petite Terre
132 and below the volcanic ridge (Lemoine et al., 2020; ReVoSiMa, 2021).

133 Our first petrological study was focused on the lavas erupted at the active volcanic site,
134 which represent an evolved basanite endmember (Berthod et al., 2021). The goal of this study

135 is to explore the most silicic (phonolite) endmember and the link between both endmembers
136 to constrain the conditions of magma storage, evolution and ascent along the ridge. Our data
137 contribute to image the magmatic system feeding the volcanic ridge east of Mayotte and to
138 constrain the possible future volcanic hazards all along the Mayotte volcanic ridge.

140 3. Methods

141 1.1. Samples and dredges

142
143 Samples from the active submarine volcanic ridge on the East flank of Mayotte Island
144 were recovered from water depths ranging from 3,200 to 1,000 m by the *R/V Marion*
145 *Dufresne* in May, June and July 2019, during oceanographic cruises MAYOBS 1, 2 and 4
146 (Feuillet, 2019; Fouquet and Feuillet, 2019; Jorry, 2019). In addition to those realized on the
147 eruptive site (MAY01-DR01, MAY02-DR08, MAY04-DR10, MAY04-DR11 and MAY04-
148 DR12, Fig. 1b, Berthod et al., 2021), dredges have been performed on four strategic sites
149 identified from high-resolution bathymetric survey of the entire volcanic ridge (Fig. 1 and
150 Tab. 1). The dredged samples were recovered in the proximal part, 10 – 15 km east of Petite
151 Terre Island, on and near a site informally nicknamed “Horseshoe” due to the horseshoe-
152 shape of the submarine volcanic feature (MAY01-DR02, MAY02-DR06, MAY02-DR07 and
153 MAY04-DR09). Three dredges collected samples from individual volcanic cones (MAY01-
154 DR02, MAY02-DR06 and MAY04-DR09). One dredge (MAY02-DR07), was performed on
155 a highly-reflective lava flow on the southeastern part of the “Horseshoe” site (Fig. 1b).
156 Dredged samples were observed and described onboard. We selected unaltered samples with
157 representative morphologies and textures, including quenched pillow rims, pillow cores, and
158 samples containing xenoliths and crystals.

159
160 With the notable exception of MAY02-DR06, each dredge collected a very homogeneous
161 set of rock types, a priori sourcing the same volcanic unit. Individual volcanic cones sampled
162 by dredges MAY02-DR06 and MAY04-DR09, are built from lavas characterized by the
163 presence of a chilled margin (1 – 2 cm thick), and an inward increase in vesicle density. A
164 few crystals are observed in MAY02-DR06 and MAY04-DR09 samples. MAY01-DR02 and
165 MAY02-DR07 samples display a glassy thick chilled margin (~ 4 cm), characterized by a
166 rounded, cracked surface and sharp conchoidal fractures. The internal part presents a bedded
167 aspect, which is delimited by elongated and flattened vesicles. These vesicles can reach
168 several centimeters in length and are organized in the plane parallel to the surface of the

169 sample. Importantly, this facies is also observed in some samples from the MAY02-DR06
170 dredge.

171 Samples collected on Petite Terre island are also used for comparison and include a
172 phonolitic glassy sample from the Vigie maar (MAY181215-14b, surrounding a large
173 ultramafic xenolith - MAY181215-14a) and a mafic crystal-rich lithic fragment from a
174 phonolitic pyroclastic deposit at Moya maar (MAY181214-02) that represents the island's
175 basement. Angular, decametric to centimetric mantle xenoliths are found in pyroclastic
176 phonolitic deposits from la Vigie (MAY181215-14a, MAY190911-4a, MAY190911-4b,
177 MAY190911-4c, MAY190911-4d) and Dziani (MAY190911-6a) phonolitic maars on Petite
178 Terre. Smaller xenoliths (cm to mm-sized) are also found in the phonolitic lava flow sampled
179 by dredge MAY02-DR07 (MAY02-DR070207E, MAY02-DR070208E).

181 *1.2. Bulk-rock analysis*

182 Bulk rock compositions were obtained on samples distributed between four dredges
183 and two sampling sites on Petite Terre (Fig. 1b). Major elements were analyzed by ICP-AES
184 on a set of 7 samples at Laboratoire Magmas et Volcans (LMV, Clermont-Ferrand, France).
185 Powdered samples were melted with LiBO_2 in a magnetic induction oven at 1100 °C for 5
186 min using graphite crucibles. The glass beads were then dissolved in a solution of deionized
187 water and nitric acid (1 M) and diluted by a factor of 2000 to produce the solution analyzed
188 by a HORIBA-Jobin-Yvon ULTIMA C ICP-AES. Analytical uncertainties ($\pm 2\sigma$) range
189 between 1 and 3% except for Na_2O (7%) and P_2O_5 (10%). Four other samples (MAY181214-
190 02, MAY181215-14b, MAY02-DR060201, and MAY02-DR060204) were analyzed at
191 plateforme "Rayons X"- Université de Paris, with an X-ray fluorimeter Epsilon 3xl (Malvern-
192 Panalytical) equipped with an Ag X-ray tube operating under He atmosphere, with
193 4 conditions during 120s: 5 kV– 60 μA without filter for the analysis of Na, Mg, Al and Si, 10
194 kV – 30 μA with a 7 μm titanium filter for the analysis of P, 12 kV – 25 μA with a 50 μm
195 aluminium filter for the analysis of Ca, K and Ti, and 20 kV – 15 μA with a 200 μm
196 aluminium filter during 120 s for the analysis of Mn and Fe. In order to avoid matrix and
197 grain size effects, all samples were melted into "beads" prepared by mixing 0.1136 g of
198 sample, 1.2312 g of fluxing agent ($\text{LiBO}_2/\text{Li}_2\text{B}_4\text{O}_7$) and 0.0187 g of non-wetting agent (LiBr)
199 in a platinum crucible. The mixture was heated to 1050 °C for 25 minutes in a fusion
200 instrument (LeNeo fluxer, Claisse). Calibration curves were obtained from identical beads of
201 14 geological reference materials (ACE, ANG, BCR-2, BEN, BHVO-2, BIR-1, BXN, DTN,
202 FKN, GSN, MAN, Mica-Fe, Osh BO, UBN and BR24). The curves are perfectly linear over

203 the entire concentration range. Analytical uncertainties ($\pm 1\sigma$) are <5% for TiO₂, MnO and
204 Fe₂O₃, 5% for MgO, SiO₂ and CaO, 10% for Al₂O₃, P₂O₅ and K₂O and 20% for Na₂O.

205 Trace elements analyses were performed by ICP-MS at Institut de physique du globe
206 de Paris (IPGP, Paris, France). Around 50 mg of powdered rock samples were digested using
207 a mix of 2 ml concentrated HNO₃ and 1 ml concentrated HF, heated in closed Teflon vessels
208 at 110°C for 24 h. An additional 3 ml of concentrated HNO₃ was added to the samples after
209 cooling and the mix was heated for another 24 h at 110 °C. Finally, 45 ml of ultrapure water
210 was added to the samples after cooling and the solutions were sonicated for 4 hours. Samples
211 were analyzed 24 to 48 hours later, after an additional 10x dilution with ultrapure water, using
212 an inert introduction system on an Agilent 7900 ICP-MS. Calibration of rock samples was
213 done against a BEN rock standard (Jochum et al., 2016). Analytical uncertainties are 6% or
214 less for lithophile elements and 15% or less for chalcophile elements.

215 *1.3. Electron microprobe analyses*

216 Composition of minerals and glasses were analyzed using the CAMECA SXFive
217 Tactis electron microprobe at LMV. We used an accelerating potential of 15 kV and a probe
218 current of 15 nA (8 nA for glasses) for major and minor elements, with 10 s counting times.
219 The beam was focused for minerals and defocused to a 20 μm diameter for glasses to avoid
220 Na migration under the electron beam. Natural and synthetic mineral standards, including
221 orthoclase (K, Al), albite (Na), wollastonite (Si, Ca), fayalite (Fe), forsterite (Mg), TiMnO₃
222 (Ti, Mn), NiO (Ni), Cr₂O₃ (Cr), and fluorapatite (P) were used for routine calibration.

223 **4. Results**

224 **4.1. Whole-rock geochemistry**

225 *Major elements*

226 Major element compositions are presented in Supplementary Tab. 1. Lavas from Mayotte
227 volcanic ridge belong to the moderately silica-undersaturated trend identified for the Comoros
228 magmas on Mayotte Island and at Karthala volcano on Grande Comore Island (Bachelery et
229 al., 2016; Pelleter et al., 2014). The distribution of lava compositions is bimodal, with
230 basanites sampled both in the distal (active eruptive site, Berthod et al., 2021) and proximal
231 part of the ridge (MAY02-DR06, MAY04-DR09), and phonolites sampled in three dredges on
232 the proximal part of the ridge (MAY01-DR02, MAY02-DR06, MAY02-DR07). Mafic

237 seamounts, with a SiO₂ content of 43.6 – 46.6 wt% and Na₂O+K₂O = 6.2 – 7.9 wt% plot in
238 the basanite/tephrite field of the TAS diagram (Fig. 2a), and according to their normative
239 olivine content should be classified as basanites. Their low MgO contents, between 4.5 and
240 6.4 wt%, and high FeO contents, 10.8 and 13.7 wt%, make them evolved basanites (Fig. 2b).
241 Basanitic samples from the two dredges (MAY04-DR09 and MAY02-DR06) scattered along
242 the ridge are very similar to lavas emitted at the 2018-2021 eruption site (Berthod et al. 2021,
243 Fig. 2a). As already observed for the eruptive site (Berthod et al. 2021), evolved basanites of
244 the volcanic ridge are characterized by an enrichment in P₂O₅ (0.9 – 2.0 wt%) compared to
245 subaerial lavas from the Comoros archipelago (Supplementary Tab. 1). The basanitic sample
246 collected on Petite Terre (MAY181214-02) display similar compositions with SiO₂,
247 Na₂O+K₂O, and MgO contents of 41.9 wt%, 2.9 wt%, and 15.4 wt%, respectively.

249 Conversely, lava flows sampled in the proximal ridge area (MAY01-DR02, MAY02-
250 DR07) and north of this site (MAY02-DR06, Fig. 1b), fall within the phonolite field of the
251 TAS diagram with SiO₂ contents ranging from 56.1 to 58.2 wt% and a Na₂O+K₂O content of
252 11.9 – 13.0 wt% (Fig. 2a). Their low MgO and FeO contents (0.47 – 0.62 % and 6.2 – 6.5 %,
253 respectively) reflect their differentiated character (Fig. 2b). The sample collected on Petite
254 Terre (MAY181215-14b) also plots in the phonolite field with SiO₂, Na₂O+K₂O and MgO
255 contents of 57.8 wt%, 5.6 wt%, and 1.2 wt%, respectively.

256 Only the largest mantle xenolith (MAY181215-14a) has been analyzed for bulk
257 chemistry, and is characterized by a high MgO content of 46.7 wt% and a low alkali content
258 of 0.36 wt%.

260 Trace elements

261 The chondrite normalized rare earth element (REE) patterns of the basanitic and
262 phonolitic samples are distinct (Fig. 3a) with different concentrations and show a strong
263 enrichment in light REE (LREE) compared to heavy REE (HREE). However, we note that
264 phonolites are more fractionated in LREE while basanites are more fractionated in HREE.
265 LREE/HREE ratios are lower in phonolites ((La/Yb)_{C1} = 17.45 – 22.97) than in basanites
266 ((La/Yb)_{C1} = 21.93 – 27.87). The phonolite REE patterns crosscut those of the basanites in
267 the middle to heavy REE range. In addition, contrary to the basanites, phonolites are
268 characterized by negative europium anomalies.

269 Basanites and phonolites display different spider diagrams of incompatible trace
1 270 elements normalized to chondrite concentrations (Fig. 3b). In particular, phonolites are
2
3 271 characterized by depletions of TiO₂, Sr, and, for some of them, Ba, compared to basanites.
4

5 272 Phonolites are more enriched in incompatible elements than basanites (Fig. 3c).
6
7 273 Indeed, Th content vary from 5 to 9 ppm in basanite and from 15 to 24 ppm in phonolite.
8
9 274 With Co content of 24 – 50 ppm in basanite and of < 1 ppm in phonolite, all samples are
10
11 275 characterized by a well-defined trend of decreasing Co with decreasing MgO content (Fig.
12
13 276 3d). This is true for all other compatible elements (Cr, Ni...). Scandium contents, ranging
14
15 277 from 12 to 16 ppm, do not vary between basanites and phonolites (Fig. 3e). Barium content
16
17 278 decrease from 1833 to 329 ppm with increasing SiO₂ content (Fig. 3f).
18

19 279 Phonolite samples collected on Petite Terre display compositions close to submarine
20
21 280 phonolites with Th, Co, Sc and Ba of 19 ppm, 1 ppm, 15 ppm and 48 ppm, respectively (Fig.
22
23 281 3). The REE pattern is similar except for the Europium anomaly which is more pronounced.
24
25 282 The basanitic sample is characterized by similar Th and Co content (4 ppm and 60 ppm,
26
27 283 respectively) and higher Sc content (45 ppm) and a lower Ba content (200 ppm) compared to
28
29 284 offshore basanites.
30

31 286 4.2. Petrology

32
33 287

34 288 The evolved basanites (MAY02-DR06 and MAY04-DR09) sampled at shallower water
35
36 289 depth on the proximal part of the ridge and the mafic clast found scattered in the Moya
37
38 290 phonolite maar (MAY181214-02) display a porphyritic texture with olivine and
39
40 291 clinopyroxene crystals set in microcrystalline groundmasses (Fig. 4a, b, and c). These evolved
41
42 292 basanites contain numerous glomerocrysts of olivine and clinopyroxene, with frequent normal
43
44 293 zoning. Some clinopyroxene crystals also show sector-zoning (MAY02-DR06 samples).
45
46 294 Olivine and clinopyroxene crystals are sometimes intergrown (Fig. 4b) indicating co-
47
48 295 crystallization of these two phases. The groundmass consists of < 150 μm subhedral
49
50 296 clinopyroxene microlites, which are occasionally zoned, and < 50 μm oxides. A few
51
52 297 clinopyroxene glomerocrysts are characterized by three stages of growth including a rounded
53
54 298 core surrounded by a rim with two stages of growth. The last stage is occasionally dendritic as
55
56 299 observed in sample MAY02-DR060201m (Fig. 4a).
57

58 301 Dredged phonolites are characterized by a trachytic texture with < 200 μm iron-rich
59
60 302 olivine (fayalite) microphenocrysts (Fig. 5). They have rounded (Fig. 5a) and/or skeletal (Fig.
61
62
63
64
65

303 5b) shapes and are intergrown with apatite and oxide crystals (Fig. 5c). The groundmass is
1 304 composed of thin < 200 μm elongated alkali feldspars, < 100 μm apatite laths and < 50 μm
2 305 euhedral oxide microlites (Fig. 5a, b, and c). There are two generation of feldspars in some
3 306 samples (Fig. 5b), with rare microphenocrysts and elongated microlites. One sample
4 307 (MAY02-DR070207) contains a few large (> 5 mm) rounded sanidine xenocrysts.
5 308

9 309 Glassy samples collected on land on Petite Terre show a similar trachytic texture and
10 310 similar mineralogy. There, subhedral iron-rich olivine crystals are set in a groundmass
11 311 containing < 50 μm feldspar microlites associated with small oxides (Fig. 5d).
12 312

16 313 Phonolitic samples (MAY02-DR07 offshore and MAY181215-14b on land) contain
17 314 mantle xenoliths that range in size from a few mm (Fig. 4d) to more than 8 cm. Ultramafic
18 315 xenoliths embedded in phonolites are mostly composed of large olivine and orthopyroxene
19 316 crystals and small clinopyroxene and spinel crystals (Fig. 4d, e and f). Some of the
20 317 orthopyroxene and clinopyroxene crystals contain exsolution lamellae (Fig. 4e and f). One of
21 318 the xenoliths (MAY02-DR070208E) is crosscut by a vein containing phlogopite, pargasitic
22 319 amphibole and a Ca-rich feldspar (Fig. 4d). The xenoliths are not in equilibrium with their
23 320 host phonolite and are surrounded by a reaction rim (Fig. 4d). Reaction between olivine
24 321 crystals and the phonolitic melt results in an overgrowth of new olivine enriched in iron,
25 322 whereas reaction between orthopyroxenes and the phonolitic melt produces a thicker reaction-
26 323 zone containing small olivine and oxide crystals.
27 324

38 324 4.3. Phase compositions and equilibria

42 326 Basanites

44 327 Basanites from dredge MAY02-DR06 are almost aphyric, and the small number of
45 328 phenocrysts show evidence of disequilibrium. Olivine phenocrysts are normally zoned, with a
46 329 sharp transition between a rounded Mg-rich core ($\text{Fo}_{80.5-84.7}$) and a rim enriched in Fe ($\text{Fo}_{72.1-}$
47 330 74.0 , Fig. 6a, Supplementary Tab. 2). According to Fe/Mg Kd, the rims are in equilibrium with
48 331 the bulk rock composition whereas the cores are not, pointing to a xenocrystic/antecrystic
49 332 origin for the cores. Clinopyroxene phenocrysts are also characterized by rounded cores (Fig.
50 333 6b, Supplementary Tab. 3), surrounded by a sieve-textured inner rim, and an outer rim with
51 334 oscillatory zoning. Magnesian cores (Mg# 70.6 – 81.9) are generally enriched in Al (up to 8.8
52 335 wt% Al_2O_3) and Na (up to 1.33 wt% Na_2O), and are again not in equilibrium with the bulk
53 336 rock composition. Rims (Mg# 67.6 – 76.4) have lower concentrations of Al (3.3 – 7.8%) and
54 337

337 Na (0.4 – 0.8 %). In one crystal, the Mg# 73 core contains inclusions of an aluminous spinel
338 (spinel-hercynite solid solution) and amphibole (hastingsite). Oxide crystals are
339 titanomagnetites with 62.8 – 69.3 % FeO and 12.6 – 19.3 % TiO₂ (Fig. 6c, Supplementary
340 Tab. 4).

341
342 As for MAY02-DR06, olivine crystals in MAY04-DR09 samples are normally zoned,
343 with a progressive compositional variation from Fo_{85.3} to Fo_{78.7} (Fig. 6a). The highest values
344 indicate that olivine cores are not in Fe/Mg equilibrium with the bulk rock, pointing to partial
345 accumulation of olivine and clinopyroxene, as suggested by the presence of glomerocrysts.
346 Clinopyroxene crystals are also normally zoned, but with more discrete variations and some
347 amount of oscillatory zoning, and Mg# variations from 85.5 down to values as low as 59.4
348 (Fig. 6b). A few crystals contain rounded cores corresponding to the most magnesian
349 compositions. Also, most of the crystals are characterized by sector zoning. As described by
350 Ubide et al., (2019), Neave et al. (2019) and Haddadi (2016), the hourglass sectors are
351 depleted in minor elements (Ti, Al, Mn, Na, and in our case also Fe), and comparatively
352 enriched in Mg compared to the prism sectors. Oxide crystals are titanomagnetites with 47.5 –
353 68.5 % FeO and 6 – 15.6% TiO₂ (Fig. 6c). A few chromium-rich spinels with Cr₂O₃ ranging
354 from 12.5 to 21.8% also occur as inclusion in some clinopyroxene crystals.

355 The basanite sample from Petite Terre, MAY181214-02 is significantly enriched in
356 large clinopyroxene and olivine crystals. Olivine crystals present a restricted compositional
357 range (Fo_{77.7} – 86.6, Fig. 2b). Contrary to samples MAY02-DR06 and MAY04-DR09, olivine
358 cores could be close to equilibrium with the bulk rock (Fe/Mg olivine Kd~0.38) but textural
359 evidence again suggest significant accumulation. Clinopyroxene crystals in this sample are
360 similar to those in MAY02-DR06 and MAY04-DR09 samples, with large variations of Mg#
361 (from 41.8 to 87.9, Fig. 6b) and Al₂O₃ (2.7 – 12.2 wt%). Most clinopyroxene crystals are
362 normally zoned, with a rather abrupt and partially rounded transition between Mg# ~85 cores
363 and more Fe-rich rims (Mg#69-78), suggesting accumulation of Mg-rich antecrysts. One
364 normally zoned crystal containing large apatite inclusions is less magnesium-rich, with a Mg#
365 between 71 and 65.

366 Phonolites

367
368 Olivine crystals in submarine and subaerial phonolites are fayalites (Fo_{17.6} – 31.6 and
369 Fo_{10.1} – 12.3 respectively) with 2.3 – 3.4 and 5.1 – 5.6 wt% MnO (Fig. 6a). They are intergrown
370 with titanomagnetite (up to 18 wt% TiO₂) and apatite. Titanomagnetite crystals contain 72.1 –

371 78.4 wt% FeO, 10.4 – 18.3 wt% TiO₂, and 2.3 – 3.4 wt% Al₂O₃ (Fig. 6c). Alkali feldspars are
372 mostly anorthoclase (Ab_{49.1 – 71.8}) with An and Or contents ranging from 3.0 to 23.8 wt% and
373 from 10.1 to 44.1 % (Fig. 6d, Supplementary Tab. 5).

374 Except for P₂O₅ content, compositions of the glasses in most samples display a trend
375 approximating a “liquid line of descent” (Fig. 2). The silica content in dredged phonolites
376 glasses (MAY02-DR06, MAY01-DR02 and MAY02-DR07 dredges) varies from 56.8 to 60.5
377 % and MgO from 0.19 to 0.41 %. As SiO₂ increases, alkalis (Na₂O + K₂O) increase from 8.7
378 to 14.1 % and FeO content decreases from 6.4 to 4.4 wt%, respectively. Glasses from
379 phonolites collected on Petite Terre Island present similar but more clustered compositions
380 with SiO₂, MgO, alkalis and FeO contents of 57.6 – 60.1 %, 0.01 – 0.08 %, 14.4 – 15.1 %, and
381 and 4.5 – 4.8 %, respectively.

383 Xenoliths

384 Ultramafic xenoliths in phonolite lavas and pyroclasts are mantle fragments
385 (harzburgite) dominated by Mg-rich olivine and orthopyroxene, with minor clinopyroxene
386 and spinel. Fo_{90.2 – 93.1} olivine contain very little MnO (0.03 – 0.22 wt%) and low CaO
387 concentrations (0-0.15 wt%), consistent with a mantle origin. Pyroxenes are Mg_{#91.3 – 94.9}
388 clinopyroxene and Mg_{#88.6 – 95.1} orthopyroxene with CaO content of 17.1 – 24.8 % and 0.37 –
389 2.53 wt%, respectively. Oxides are chrome-spinel with Cr₂O₃ higher than 31% and FeO
390 content ranging from 17.0 to 24.3 wt%. In one xenolith sample (MAY02-DR070208E), a vein
391 contains a few crystals of bytownite plagioclase (An_{76.7 – 79.7}), pargasitic amphibole (Mg_{# 92})
392 and phlogopite mica (Mg_{# 91.2 – 93.2}).

394 **5. Discussion**

395
396 Both phonolites and basanites are present on the proximal part of the volcanic ridge and
397 onshore, on Petite Terre Island. Phonolites and basanites collected offshore and on land
398 display similar textural, petrological and geochemical features (Figs 2 – 6). Proximal
399 basanites have a porphyritic texture with a microcrystalline groundmass made of
400 clinopyroxene microlites and Fe-Ti oxides (Fig. 4a, b, and c), and glomerocrysts of zoned
401 olivine and sector-zoned clinopyroxene. By contrast, the eastern part of the submarine ridge is
402 only built from basanites characterized by an aphyric texture (ongoing eruptive site, Berthod
403 et al., 2021).

404 All these samples belong to a moderately silica-undersaturated alkaline series (Fig. 2)
1 405 which corresponds to the Karthala trend (Bachèlery and Hémond, 2016). Also,
2 406 geographically, all samples belong to a N140 alignment of numerous volcanic features (Fig.
3 407 1b, (Feuillet et al., 2021)). This 60 km long volcanic ridge runs on the eastern flank of
4 408 Mayotte, from the site of a large active 2018-ongoing submarine eruption to the east, to Petite
5 409 Terre Island to the west (Fig. 1b). The existence of this ridge raises two main scientific
6 410 questions: (1) What is the origin of the phonolites, are they related to the basanites? (2) Is the
7 411 entire volcanic ridge, on land and offshore, fed by the same plumbing system or are there
8 412 numerous ascent pathways and magma storage zones? To answer these questions, it is
9 413 necessary to understand how this compositional bimodality is achieved.

18 414 Since the phonolites contain mantle xenoliths (Fig. 4d, e and f), they were generated
19 415 below the Moho, i.e., deeper than 17 km (Dofal et al., 2018). Most phonolites are generated
20 416 by fractional crystallization in shallow crustal magma chambers (< 10 km, Grant et al. 2013
21 417 and references therein), and evidence for phonolitic melts at mantle depth is scarce (e.g., Price
22 418 and Green 1972; Dautria et al., 1983; Grant et al. 2013). It has been demonstrated that
23 419 phonolites can be directly produced by mantle melting (Irving and Price, 1981; Laporte et al.,
24 420 2014; Loges et al., 2019). Such phonolites have low FeO concentrations (2 – 3 wt%) and are
25 421 in equilibrium with high Mg# olivines (~Fo₉₀, Laporte et al. 2014). Phonolitic glass in
26 422 equilibrium with mantle compositions have been analyzed in lherzolitic mantle xenoliths from
27 423 La Grille on Grande Comore (Coltorti et al. 1999), and indeed show high Mg# (59 – 78) and
28 424 low FeO concentrations (<3.1 wt%). The investigated phonolites of the Mayotte ridge,
29 425 however, are highly evolved, with a significant enrichment in FeO (6.1 – 6.5 wt%) and are in
30 426 equilibrium with low Mg# olivines (Fo_{13–28}), precluding an origin by direct mantle melting.
31 427 The differentiated character of those phonolites would thus be better explained by fractional
32 428 crystallization of a more primitive magma in a mantle reservoir.

47 430 **5.1. Evidence of fractional crystallization**

49 431
50 432 No primitive composition in equilibrium with a mantle lherzolite has been erupted
51 433 along the ridge. This indicates the presence of one or more reservoirs in which the magma
52 434 evolves between the source and the surface. According to our previous studies (Berthod et al.
53 435 2021; Feuillet et al. 2021), there are at least two levels of magma storage, one near 40 - 50 km
54 436 depth in which the primitive magma differentiated to form the evolved basanites, and one
55 437 upper level, possibly between 15 and 20 km where some more evolved magma is stored.

438 The evolution of igneous suites by fractional crystallization is characterized by
1 439 decreasing compatible trace elements whereas incompatible elements increase and have
2
3 440 constant ratios with each other (Kyle et al., 1992). According to our major and trace elements
4
5 441 data, the fractionating assemblage likely includes clinopyroxene (decrease in CaO and Sc,
6
7 442 Fig. 2c and 3e), feldspar (negative Eu anomaly, decrease in Ba and Sr, Fig. 3), magnetite and
8
9 443 ilmenite (decrease in FeO, TiO₂, and Co, Figs 2 and 3), apatite (strong decrease in P,
10
11 444 Supplementary Tab. 1) and possibly olivine (decrease in MgO, Ni and Co, Figs 2 and 3).
12
13 445 There is no evidence for the crystallization of hydrous minerals (amphibole, mica), which
14
15 446 usually produce negative anomalies in K₂O, Rb, and High Field Strength Elements like Nb,
16
17 447 Ta, Zr and Hf (Matsui et al., 1977; Schnetzler and Philpotts, 1970).

18 448 The volcanism of the ridge extending from Petite Terre to the 2018 - 2021 eruption site
19
20 449 is strongly bimodal, and no intermediate composition between evolved basanites and
21
22 450 phonolites have been sampled so far despite three dredging campaigns and two sampling
23
24 451 missions on land. This compositional gap commonly observed in tholeiitic and calc-alkaline
25
26 452 series (e.g., Daly (1925), Grove and Donnelly-Nolan (1986), Reubi and Blundy (2009)) is
27
28 453 rarely observed in alkaline series. This feature complicates petrological modelling, but does
29
30 454 not in any way precludes an origin for the phonolites by differentiation of the basanites.

31 455 The possibility of a genetic link between basanites and phonolites was tested through
32
33 456 a series of fractionation models: (1) Melts model, for major elements coupled with mass
34
35 457 balance and (2) trace element correlation model.

36 458

38 459 **5.2. Fractional crystallization tested with MELTS models and mass balance**

39

40 460

41

42 461 Fractional crystallization models were run using the Rhyolite-MELTS software
43
44 462 (Ghiorso and Gualda, 2015; Ghiorso and Sack, 1995; Gualda et al., 2012). We used the bulk
45
46 463 composition of evolved basanite MAY01-DR0105 collected at the 2018-2021 eruption site, as
47
48 464 parental melt, including 2.3 wt% H₂O as measured in olivine-hosted melt inclusions (Berthod
49
50 465 et al. 2021). For each model, temperature decreased from 1200 to 700 °C, with a 10 °C step.
51
52 466 Since no orthopyroxene and garnet crystals were found in Comoros lavas, they were excluded
53
54 467 from the crystallizing assemblage. We tested a range of possible pressures from 0.4 to 1.2
55
56 468 GPa, H₂O concentrations from 1.0 wt% to 5.0 wt%, and a range of oxygen fugacities buffered
57
58 469 between FMQ+1 and FMQ-2. Results of our Rhyolite-MELTS models are presented on Fig.
59
60 470 7. All models are mainly characterized by early crystallization of clinopyroxene, apatite and
61
62 471 magnetite starting above 1100 °C. A second crystallization stage involves anorthoclase and

472 biotite with very late-stage leucite in some models. Early crystallization of olivine appears at
1 473 low pressure and low oxygen fugacity. Ilmenite crystallizes in all models with $H_2O \leq 3.0 \%$
2 474 and generally appears early at high pressure and low oxygen fugacity. We observed that
3 475 changes in initial H_2O concentration decreases the crystallization temperatures but only have
4 476 a limited impact on the crystallization path. An increase in pressure produces a strong
5 477 increase in FeO and Na_2O concentrations (Fig. 7). This is correlated with the involvement of
6 478 more clinopyroxene, particularly early on, a decrease in magnetite and ilmenite contents, and
7 479 absence of olivine. Variations in oxygen fugacity have a similar impact to pressure, with
8 480 lower oxygen fugacity decreasing the amount of clinopyroxene and magnetite and resulting in
9 481 higher FeO and Na_2O contents. Therefore, the exceptional FeO content in Petite Terre and
10 482 submarine ridge phonolites (Fig. 7) may be a consequence of a deeper fractionation level
11 483 compared to most phonolites (Grant et al., 2013; Moussallam et al., 2013; Scaillet et al.,
12 484 2008) and/or particularly low oxygen fugacity. This observation is supported by the fact that
13 485 the best fits to the phonolite composition are obtained at the highest pressures and lowest
14 486 oxygen fugacities. The overall best model is obtained at 0.6 GPa with 2.3 wt% H_2O and an
15 487 oxygen fugacity of FMQ-1 (Fig. 7), with a crystallizing assemblage of olivine (12.5 %),
16 488 magnetite (15.5 %), apatite (5 %), ilmenite (4 %) and clinopyroxene (34 %) at high
17 489 temperature, and anorthoclase (30%) below 1000 °C. Further crystallization after reaching the
18 490 composition of MAY02-DR07 / MAY01-DR02 phonolites produces biotite, anorthoclase and
19 491 leucite. Small amounts of fayalite crystallize in the lower oxygen fugacity models (FMQ-1
20 492 and lower). The presence of fayalite microlites in the phonolites is thus likely indicative of
21 493 low oxygen fugacity, as confirmed by experimental studies (Giehl et al., 2013; Romano et al.,
22 494 2020; Rutherford, 1969).

495
496 The phonolites from the ridge are characterized by an unusual enrichment in iron,
497 compared to older phonolites from the main island of Mayotte (Debeuf, 2004; Pelleter et al.,
498 2014), and most phonolites worldwide (Fig. 7). This iron enrichment, akin to the trend
499 observed in the tholeiitic series (e.g. Carmichael 1964) has already been described in some
500 lavas from the East African Rift (Barberi et al., 1971; Nash et al., 1969) and in the peralkaline
501 rocks of the Gardar province in Greenland (Marks and Markl, 2003). Iron enrichment is
502 usually explained by a late involvement of magnetite in the crystallization sequence (Chin et
503 al., 2018; Luhr et al., 1984), possibly a consequence of low oxygen fugacity (e.g., Marks and
504 Markl 2003, Nash et al. 1969) and/or low water content (Tatsumi and Suzuki, 2009). These

505 observations are in agreement with the Rhyolite-MELTS model, which suggests reducing
1 506 conditions, and magma storage and evolution at upper mantle levels.

3 507
4
5 508 To confirm the Rhyolite-MELTS model, we performed a simple least-squares mass
6
7 509 balance using major elements (Bryan et al. 1969). The calculation starts from the same
8
9 510 composition (MAY01-DR0105 sample, Berthod et al. 2021) and ends with the composition of
10
11 511 MAY01-DR020202 phonolite. We use microprobe analyses of phenocrysts and microlites
12
13 512 from MAY01-DR0105 (olivine, clinopyroxene, magnetite, apatite), MAY02-DR08 (ilmenite)
14
15 513 and MAY01-DR02 (anorthoclase and fayalite). The best model implies the crystallization of
16
17 514 anorthoclase (50%), olivine (18 %), clinopyroxene (15 %), magnetite (8 %), apatite (5 %),
18
19 515 and ilmenite (4 %).

20 516 21 22 517 **5.3. Fractional crystallization tested with trace elements model**

23 518
24
25 519 Trace element compositions of basanites found along the submarine ridge are similar to
26
27 520 those reported for the 2018 - 2021 ongoing eruption (Fig. 3b, Berthod et al. 2021), and for the
28
29 521 entire Comoros archipelago (Bachelery and Hémond, 2016; Class et al., 1998; Claude-Ivanaj
30
31 522 et al., 1998; Deniel, 1998b; Späth et al., 1996).

32
33 523 REE are strongly fractionated ($(La/Yb)_{pm} = 21.9 - 27.9$), indicating a deep peridotitic
34
35 524 source with residual garnet, in agreement with previous studies on subaerial Comoros lava
36
37 525 that propose a depth of partial melting near the spinel / garnet boundary, i.e. 80 – 100 km,
38
39 526 (Bachelery and Hémond, 2016; Class et al., 1998; Claude-Ivanaj et al., 1998; Deniel, 1998b;
40
41 527 Späth et al., 1996) and our previous study of the ongoing 2018-2021 eruption (Berthod et al.,
42
43 528 2021).

44 529 Phonolite and basanite lavas display similar REE enrichment but with significantly
45
46 530 different patterns (Fig. 3a and b). In fact, phonolite REE patterns are less fractionated than the
47
48 531 basanites ($(Gd/Y)_{pm} = 3.2 - 5.1$), which could suggest a different shallower source within the
49
50 532 spinel stability field (Fig. 8a). In addition, if phonolites are derived from basanites by
51
52 533 fractional crystallization, REE patterns should be more enriched than the mafic parental
53
54 534 magma. To obtain similar patterns, the fractionated assemblage must include a REE-rich
55
56 535 mineral that preferentially fractionate middle REE. All basanitic samples are characterized by
57
58 536 an excess of phosphorus, also observed in all glass analyses (Fig. 8a), suggesting that apatite
59
60 537 crystallization might play a role. In fact, apatite melt partition coefficients can reach high
61
62 538 values (up to 21.7 for La, Luhr et al. 1984; Fujimaki 1986; Mahood and Stimac 1990;

539 Prowatke and Klemme 2006). Using these high partition coefficients and estimated amount of
1 540 fractionated apatite from phosphorus concentration, we can reproduce the phonolite REE
2 541 pattern (Fig. 8b, and Supplementary Tab. 6). Therefore, we suggest that REE ratios do not
3 542 reflect a different source but are solely a consequence of apatite crystallization.
4
5
6

7 543
8
9 544 Phase proportions in the fractionated assemblage were estimated using the model
10 proposed by Villemant et al. (1981). In their model, bulk partition coefficients in a
11 545 monotonous fractionation series are calculated from the log/log plots of trace elements versus
12 546 Th, taken as a perfectly incompatible reference element. In Mayotte samples, a few elements
13 547 (Nb, Ta, Zr, Cs) are more incompatible than Th, so we used Cs, the most incompatible
14 548 element, instead of Th. This is usually not done because of the high mobility of Cs, however,
15 549 given the very young age of the investigated rocks, there is a very good correlation between
16 550 Cs and Th ($r^2 = 0.972$) indicating that Cs mobility was negligible. We then selected a series of
17 551 trace elements for which (1) the correlation with Th and Cs is good ($r^2 > 0.90$) or the value is
18 552 constant, and (2) there is a good set of mineral/melt partition coefficient available (partition
19 553 coefficients taken from Adam and Green (2006), Stix and Gorton (1990), Klemme et al.
20 554 (2006) and Mahood and Stimac (1990)). We then performed a multiple regression analysis
21 555 following Villemant et al. (1981) to extract the proportions of minerals in the fractionated
22 556 assemblage, from the bulk partition coefficients and individual mineral partition coefficient.
23 557 We only use minerals that have been observed in at least one dredged sample, i.e., olivine,
24 558 clinopyroxene, magnetite, ilmenite, anorthoclase, and apatite. There is no break in slope in the
25 559 log/log correlation, suggesting that the fractionating assemblage is relatively constant, at least
26 560 within the resolution of our model, which is limited by the absence of intermediate
27 561 compositions in the phonotephrite/tephriphonolite fields. HFSE are among the most
28 562 incompatible elements, equally or more incompatible than Th, which preclude the
29 563 crystallization of amphiboles or micas. Phase proportions in the crystallizing assemblage are
30 564 dominated by feldspar (54 %), clinopyroxene (26 %), olivine (12 %), and apatite (8 %), with a
31 565 negligible amount of magnetite. These results are in good agreement with the Rhyolite-
32 566 MELTS model, and the mass-balance calculations.
33
34
35
36
37
38
39
40
41
42
43
44
45
46
47
48
49
50
51
52

53 568 54 569 **5.4. Evidence of multiple levels of magma storage**

55 570 56 571 **Basanitic mantle reservoirs**

572 As evidenced for lavas emitted by the 2018-2021 ongoing eruption on the eastern part of
1 573 the submarine volcanic ridge (Fig. 1b), the low Mg# of the basanites indicates that they are
2
3 574 not primary mantle melts (Berthod et al. 2021). This is supported by the presence of zoned
4
5 575 olivine and clinopyroxene phenocrysts, which typically grow in dynamic reservoirs
6
7 576 undergoing frequent replenishments and drainages (Fig. 4a, b, and c).

8
9 577 In addition, our barometric study of the clinopyroxene phenocrysts (Putirka, 2008)
10
11 578 indicate multiple levels of magma storage beneath the volcanic ridge (Fig. 9). Since
12
13 579 clinopyroxene compositions are neither in equilibrium with the bulk rocks nor in equilibrium
14
15 580 with the residual glasses, the Putirka (2008) clinopyroxene-only geobarometer (equation 32a)
16
17 581 is the most accurate geobarometer, with a standard error of estimate of 0.28 GPa (9 km). We
18
19 582 estimate that the cores of clinopyroxene phenocrysts (Mg#₈₂₋₇₃) in MAY02-DR06 basanite
20
21 583 sample crystallized during a first phase of growth in a basanitic magma reservoir located at
22
23 584 about 57 ± 9 km depth (Fig. 9). The location of this deep magma reservoir is in excellent
24
25 585 agreement with seismicity location (ReVoSiMa, 2021) and is consistent with the previous
26
27 586 geophysical studies (Cesca et al., 2020; Feuillet et al., 2021; Lemoine et al., 2020) and our
28
29 587 previous geobarometric study on 2018-2021 erupted lavas which proposed a ≥ 37 km deep
30
31 588 mantle reservoir (Berthod et al., 2021). Oscillatory zoned outer rims (Mg#₆₇₋₇₃) crystallized
32
33 589 during a second phase of growth in a shallower more differentiated basanitic magma chamber
34
35 590 at an average depth of 18 ± 9 km (0.47 ± 0.28 GPa, Fig. 9).

36 591 Similar results have been obtained for sector-zoned clinopyroxene glomerocrysts in the
37
38 592 MAY04-DR09 basanite sample. A few deep resorbed clinopyroxene cores (Mg#₈₃₋₈, Fig. 9)
39
40 593 crystallized at a pressure of 1.19 ± 0.28 GPa equivalent to a depth of 40 ± 9 km. For the
41
42 594 sector-zoned rims, we only used the Al₂O₃-rich prism sectors for barometry calculations,
43
44 595 since hourglass sectors have been shown to produce erroneous pressure (Neave et al., 2015).
45
46 596 Except for the resorbed cores, barometry indicate that clinopyroxene crystals (Mg#_{59-82.5})
47
48 597 formed at intermediate pressures similar to those obtained for MAY02-DR06: 0.43 ± 0.28
49
50 598 GPa (16 ± 9 km, Fig. 9).

51 599 For the MAY181214-02 basanite sample collected on Petite Terre, no evidence was found
52
53 600 for a deep fractionation level, and a mean depth of 17 ± 9 km (clinopyroxene Mg#_{47.9-67.5})
54
55 601 has been calculated from phenocrysts and rims of the zoned clinopyroxene antecrysts (Fig. 9).
56
57 602 Since MAY181214-02 ankaramite corresponds to an old lithic fragment collected on Petite
58
59 603 Terre, our results suggest a stable depth for the shallower magmatic system feeding both on
60
61 604 land and offshore part of the active volcanic ridge of Mayotte through time.
62
63
64
65

605 Our geobarometric results allow us to propose two different mantle storage levels: one
606 deep mantle storage located below 40 km (Fig. 9) and another shallower storage at about 15 –
607 20 km, near the Moho (Moho depth estimated at ~17 km, Dofal et al. 2018). However, the
608 large range of clinopyroxene compositions and zoning patterns preclude an identical transfer
609 path for each magma pulse.

611 *Phonolitic mantle reservoir*

612 Phonolitic lavas contain clinopyroxene bearing harzburgite xenoliths (Fig. 4d, e and f).
613 These fragments of mantle peridotite, incorporated into the phonolitic magma as it rose to the
614 surface, indicate that they ascended from the mantle. In order to estimate the minimum depth
615 of the phonolitic reservoir(s), we used a geothermobarometer (Putirka, 2008) on a series of
616 clinopyroxene-orthopyroxene pairs in the mantle xenoliths (Fig. 4d, e and f). These
617 geobarometric calculations also provide the maximum depth of the Moho below the
618 investigated area. Temperatures were calculated using equation (36) of Putirka et al. (2008)
619 with reported uncertainties of 45 °C (see Berthod et al., 2021 for discussion). For pressure,
620 both equations (38) and (39) were tested against experiments performed at 1.00 GPa by
621 Condamine and Médard (2014). Since equation (38) returned an average pressure of 1.02
622 GPa, whereas equation (39) returned a less accurate average pressure of 0.88, equation (38)
623 was thus preferred for the calculation. It reproduces the experimental data with an average
624 error (SEE) of 0.19 GPa. Calculations performed on clinopyroxene-orthopyroxene pairs in
625 textural equilibrium and on exsolutions (Fig. 4d-f) give identical results. Assuming an average
626 density of 2,890 kg.m⁻³ for the oceanic crust and 3,300 kg.m⁻³ for the lithospheric mantle,
627 mantle xenoliths from phonolitic pyroclastic deposits from Petite Terre were equilibrated at
628 the following depths (Fig. 9): 11.9 ± 3.4 km (MAY181215-14a), 12.3 ± 3.7 km
629 (MAY190911-6a), 18.3 ± 5.4 km (MAY190911-4a), 14.5 ± 0.4 km (MAY190911-4b), 12.4 ±
630 2.9 km (MAY190911-4c) and 14.5 ± 2.1 km (MAY190911-4d). Clinopyroxene-
631 orthopyroxene pairs were also analyzed in two more mantle xenoliths from phonolites of the
632 submarine ridge and give similar equilibration depths of 15.2 ± 2.3 km (MAY02-DR070207)
633 and 11.0 ± 1.3 km (MAY02-DR070208-xen, Fig. 9).

634 These depths are consistent with seismic data locating the Moho at about 17 km (Dofal
635 et al., 2018), with the existence of numerous very low frequency seismic events between 10
636 and 30 km depths (Laurent et al., 2019, Feuillet et al., 2021), and with magnetotelluric
637 sounding performed on the volcanic region (Darnet et al., 2020) which suggests the presence
638 of magmatic conductive fluids at depth > 15 km. This is also coherent with the presence of an

639 evolved magma batch located above 17 ± 6 km (0.45 ± 0.19 GPa) intersected by the June
1 640 2019 lava flow at the active volcanic site (sample MAY02-DR08, Berthod et al., 2021).
2
3 641 Finally, results from the Rhyolite-MELTS model confirm that differentiation occurred at
4
5 642 about 20 km depth (0.6 GPa, Fig. 7).
6

7 643 Since similar minimum storage depths have been obtained for phonolites sampled on
8
9 644 Petite Terre and on the intermediate part of the volcanic ridge. This raises the question as to
10
11 645 whether these depths correspond to a single magma reservoir or to a zone made of several
12
13 646 magma lenses. We suggest that the hundreds seamounts constituting the 60 km-long and 31
14
15 647 km-wide volcanic ridge (Fig. 1b) were probably emplaced between the last volcanic activity
16
17 648 at Petite Terre (i.e. about 4000 years ago, Zinke et al. 2003) and the currently ongoing
18
19 649 eruption. As shown by Castruccio et al. (2017), monogenetic volcanic fields are likely to be
20
21 650 fed by ephemeral superficial magmas lenses rather than long-lived reservoirs.
22

23 651 We note that the evidence of multiple magma storage can also explain the bimodal
24
25 652 volcanism. However, the minimum depth of the phonolitic storage obtained from the
26
27 653 xenoliths is similar to the shallower basanitic reservoir (Fig. 9) located at about 15-20 km
28
29 654 depth. Therefore, we can evaluate the possibility that phonolites are products of
30
31 655 differentiation of basanite magmas in the shallower reservoirs located close to the MOHO
32
33 656 seismic discontinuity interpreted as the Mantle-crust interface.
34

35 657 **5.5. Integration in the geological context of Mayotte: possible eruption triggers?**

36 658
37
38 659 Berthod et al. (2021) demonstrated that 50 % crystallization of a cumulate containing
39
40 660 80 % clinopyroxene and 20 % olivine is required to generate the basanite from a primary
41
42 661 mantle melt in the deeper mantle reservoir (below 37 km). We then propose three scenarios
43
44 662 for magma evolution beneath the volcanic ridge: (1) the basanitic magma rises directly and
45
46 663 rapidly to the surface from the deep magma reservoir as evidenced by the petrological
47
48 664 characteristics of the ongoing eruption (Berthod et al. 2021) and seismological data (Cesca et
49
50 665 al. 2020; Feuillet et al. 2021; Lemoine et al. 2020). (2) zoned clinopyroxene phenocrysts in
51
52 666 some basanitic lavas at proximal seamounts MAY02-DR06 and MAY04-DR09 and on Petite
53
54 667 Terre indicate that the basanitic magma stalls at the Moho interface before resuming its ascent
55
56 668 toward the surface. (3) the basanitic magma stops and evolves to phonolite in a reservoir
57
58 669 below the Moho. In this third scenario, the phonolitic magma might be reactivated by the
59
60 670 arrival of a deeper and more primitive magma sourced from a deep reservoir > 30 km. The
61
62 671
63
64
65

672 absence of phenocryst in the phonolites might be explained by an increase in temperature
1 673 induced by the self-mixing reactivation (Couch et al. 2001).

3 674 Our three different models show that the phonolitic lavas can be produced by
4 675 approximately 80 % fractional crystallization of a hydrous basanitic magma at mantle depths
5 676 ($P > 0.6$ GPa) under reduced oxygen fugacity (~FMQ-1). The total volume of MAY02-DR07
6 677 lava flow is estimated at 0.45 km^3 , therefore, the volume of basanite necessary to generate this
7 678 phonolitic lava flow is at least 1.6 km^3 . Taking into account the 50 % crystallization in the
8 679 deeper mantle reservoir, the eruption of 0.46 km^3 of phonolitic magmas thus requires
9 680 intrusion of 4.6 km^3 of primary mantle melts.

16 681
17 682 Since 2018, Mayotte is the site of unprecedented and unexpected volcanic and seismic
18 683 activities (Feuillet et al. 2021; Cesca et al. 2020; Lemoine et al. 2020). Following an
19 684 oceanographic campaign, Feuillet et al. (2021) demonstrated that the hundreds of seismic
20 685 events were associated with the development of a large volcanic edifice. As of January 2021,
21 686 the volcano has risen 820 m above the 3,300 m deep seafloor with an erupted lava volume of
22 687 $\sim 6.5 \text{ km}^3$ (Feuillet 2019; ReVoSiMa 2021) which represents by far the largest observed
23 688 submarine eruption (Clague et al. 2011; Resing et al. 2011; Caress et al. 2012; Chadwick et al.
24 689 2016; Carey et al. 2018; Chadwick Jr et al. 2018) and the third largest mafic eruption of the
25 690 last two millennia (Thordarson and Self 1993; Thordarson et al. 2001; Oppenheimer et al.
26 691 2018; Patrick et al. 2020). Berthod et al. 2021 demonstrated that this ongoing eruption is fed
27 692 by a deep (≥ 37 km) and large ($\geq 10 \text{ km}^3$) mantle reservoir of evolved, alkaline magma having
28 693 experienced extensive crystallization (50%).

39 694 This volcanic edifice is located on a N140 volcanic ridge that runs off the eastern flank of
40 695 Mayotte and whose subaerial expression is Petite Terre Island (Feuillet et al. 2021, Fig. 1b), a
41 696 ridge composed of hundreds of volcanic edifices (Fig. 1b). Large phonolitic lava flows are
42 697 present on this ridge, about 10-15 km East of Petite Terre (Fig. 1b). Pyroclastic phonolitic
43 698 edifices are also present on the submarine ridge and on Petite Terre. If phonolites derive by
44 699 fractional crystallization from basanitic lavas similar to those feeding the ongoing eruption,
45 700 and the structure of the plumbing system is similar all along the ridge, we suggest that the
46 701 entire volcanic ridge could be fed by the same magmatic system. Moreover, geological
47 702 mapping of the more than 300 submarine cones and vents clearly show that the zone of the
48 703 Horseshoe 5-15 km from Petite Terre is the area with the highest density of individual
49 704 eruptive vents per km^2 of the entire ridge (Fig. 1b). The extensive diversity of eruptive vents,
50 705 eruptive styles, both explosive and effusive, the magma bimodal composition, the large

706 erupted volumes and multiple superimposed eruptive cones and lava domes suggests that
1 707 volcanism in the Horseshoe area has been fed by a long-lasting and extensive transcrustal
2 708 magmatic system that forms the core of the magmatic system branching out to the West
3 709 towards the Petite Terre recent Holocene volcanic centers as well as branching out to the East
4 710 towards the rest of the chain. The results of our petrological analysis coupled with seismic
5 711 data (Cesca et al. 2020; Lemoine et al. 2020; Feuillet et al. 2021) support the hypothesis that
6 712 this transcrustal magmatic system is currently undergoing a massive reactivation that is
7 713 feeding the current exceptional voluminous submarine eruption. In such a model, existing
8 714 phonolitic magma lenses could be reactivated by reinjection of the basanitic magma feeding
9 715 the ongoing eruption (Sparks et al. 1977). Although no evidence of mingling or mixing has
10 716 been identified in the phonolites so far, the presence of reversed zoned olivine phenocrysts in
11 717 the recently erupted basanite lavas (Berthod et al. 2021) suggest that mixing involving a small
12 718 shallow differentiated magma reservoir located close to the Moho ($< 17 \pm 6$ km) did occur
13 719 beneath the current eruption site. This indicate that if eruptible magma is still present in lenses
14 720 of the transcrustal mush magmatic system located at Moho depth underneath the ridge, it
15 721 could be reactivated by the arrival of a deeper and more primitive magma. Such a scenario
16 722 would have major implications in terms of increased volcanic hazard for Mayotte on land. In
17 723 fact, more than 300,000 people are living on Mayotte with about 70,000 in the capital
18 724 Mamoudzou located within the Holocene phreatomagmatic explosive volcanic zone, and
19 725 30,000 people on Petite Terre Island which hosts the only international airport of the
20 726 archipelago, the electric plant and other economical and industrial assets as well as most of
21 727 the public administration.
22
23
24
25
26
27
28
29
30
31
32
33
34
35
36
37
38
39
40
41

42 729 6. Conclusion

43 730 Our petrological study shows that the hundreds of edifices, individual cones and lava
44 731 flows forming the active volcanic ridge on the east flank of Mayotte Island are characterized
45 732 by a bimodal chemical distribution of erupted magmas, with basanite and phonolite but no
46 733 intermediate compositions. Trace element characteristics indicate that those lavas result from
47 734 partial melting near the garnet – spinel transition zone, between 80 – 100 km, which is
48 735 consistent with the structuration of lithosphere in the region. Basanitic magmas are first stored
49 736 and evolve in a deep magma reservoir located between 35 and 57 km. Clinopyroxene
50 737 barometry highlights the existence of a second shallower storage system at about 15 – 20 km,
51 738 probably made of multiple lenses of basanitic and phonolitic magmas that form an extensive
52
53
54
55
56
57
58
59
60
61
62
63
64
65

739 and long-lasting transcrustal mush magmatic system. Basanitic magmas evolve to phonolites
740 by about 81 % fractional crystallization in this shallow storage system.

741 Three scenarios are proposed: (1) the basanitic magma can rise directly and quickly to the
742 surface from the deep magma reservoir (current ongoing activity, Berthod et al. 2021). (2) the
743 basanitic magma stalls in a shallower reservoir near the Moho before resuming its ascent
744 toward the surface. (3) the basanitic magma stops and evolves to phonolite in the shallower
745 magma storage zone. In this third scenario, the phonolitic magma might be reactivated by the
746 arrival of a new batch of deeper basanitic magma. If the entire volcanic ridge is fed by the
747 same extensive plumbing system sourcing the transcrustal mush magmatic system below the
748 Horseshoe area, 5 – 15 km East of Petite Terre, the current reinjection of basanitic magma
749 feeding the ongoing voluminous eruption could reactivate the phonolitic reservoirs that fed
750 the volcanic areas on Petite Terre and the volcanic ridge crossing the eastern flank of
751 Mayotte, drastically increasing volcanic hazards for the island of Mayotte. This is of
752 particular concern given that Berthod et al. (2021) have shown that the timescales that
753 separated the last geochemical perturbation of eruptible magma in a shallow Moho-depth
754 storage zone recorded by zoned crystals, and the arrival of the magma on the surface were on
755 the range of 30 ± 4 days.

757 **References**

- 758 Ablay, G.J., Carroll, M.R., Palmer, M.R., Martí, J., Sparks, R.S.J., 1998. Basanite–phonolite
759 lineages of the Teide–Pico Viejo volcanic complex, Tenerife, Canary Islands. *J. Petrol.*
760 39, 905–936. <https://doi.org/10.1093/petroj/39.5.905>
- 761 Adam, J., Green, T., 2006. Trace element partitioning between mica-and amphibole-bearing
762 garnet lherzolite and hydrous basanitic melt: 1. Experimental results and the
763 investigation of controls on partitioning behaviour. *Contrib. to Mineral. Petrol.* 152, 1–
764 17. <https://doi.org/10.1007/s00410-006-0085-4>
- 765 Bachèlery, P., Hémond, C., 2016. Geochemical and Petrological Aspects of Karthala
766 Volcano, in: *Active Volcanoes of the Southwest Indian Ocean*. Springer, pp. 367–384.
- 767 Bachèlery, P., Morin, J., Villeneuve, N., Soulé, H., Nassor, H., Ali, A.R., 2016. Structure and
768 eruptive history of Karthala volcano, in: *Active Volcanoes of the Southwest Indian*
769 *Ocean*. Springer, pp. 345–366.
- 770 Barberi, F., Bizouard, H., Varet, J., 1971. Nature of the clinopyroxene and iron enrichment in
771 alkalic and transitional basaltic magmas. *Contrib. to Mineral. Petrol.* 33, 93–107.
- 772 Berthod, C., Médard, E., Bachèlery, P., Gurioli, L., Di Muro, A., Peltier, A., Komorowski, J.,

- 773 Benbakkar, M., Devidal, J., Langlade, J., Besson, P., Boudon, G., Rose-Koga, E.,
1 774 Deplus, C., Le Friant, A., Bickert, M., Nowak, S., Thinon, I., Burckel, P., Hidalgo, S.,
2 775 Jorry, S., Fouquet, Y., Feuillet, N., 2021. The 2018-ongoing Mayotte submarine
3 776 eruption: magma migration imaged by petrological monitoring. Minor revisions, in
4 777 progress. *Earth Planet. Sci. Lett.*
5
6
7
8
9 778 Bertil, D., Regnault, J.M., 1998. Seismotectonics of Madagascar. *Tectonophysics* 294, 57–74.
10
11 779 [https://doi.org/10.1016/S0040-1951\(98\)00088-2](https://doi.org/10.1016/S0040-1951(98)00088-2)
12
13 780 Castruccio, A., Diez, M., Gho, R., 2017. The influence of plumbing system structure on
14 781 volcano dimensions and topography. *J. Geophys. Res. Solid Earth* 122, 8839–8859.
15 782 <https://doi.org/10.1002/2017JB014855>
16
17
18 783 Cesca, S., Letort, J., Razafindrakoto, H.N.T., Heimann, S., Rivalta, E., Isken, M.P., Nikkhoo,
19 784 M., Passarelli, L., Petersen, G.M., Cotton, F., Dahm, T., 2020. Drainage of a deep
20 785 magma reservoir near Mayotte inferred from seismicity and deformation. *Nat. Geosci.*
21 786 13, 87–93. <https://doi.org/10.1038/s41561-019-0505-5>
22
23
24
25 787 Chin, E.J., Shimizu, K., Bybee, G.M., Erdman, M.E., 2018. On the development of the calc-
26 788 alkaline and tholeiitic magma series: A deep crustal cumulate perspective. *Earth Planet.*
27 789 *Sci. Lett.* 482, 277–287. <https://doi.org/10.1016/j.epsl.2017.11.016>
28
29
30
31 790 Class, C., Goldstein, S.L., 1997. Plume-lithosphere interactions in the ocean basins:
32 791 constraints from the source mineralogy. *Earth Planet. Sci. Lett.* 150, 245–260.
33
34
35 792 Class, C., Goldstein, S.L., Altherr, R., Bachèlery, P., 1998. The process of plume–lithosphere
36 793 interactions in the ocean basins—the case of Grande Comore. *J. Petrol.* 39, 881–903.
37 794 <https://doi.org/doi.org/10.1093/etroj/39.5.881>
38
39
40 795 Class, C., Goldstein, S.L., Shirey, S.B., 2009. Osmium isotopes in Grande Comore lavas: a
41 796 new extreme among a spectrum of EM-type mantle endmembers. *Earth Planet. Sci. Lett.*
42 797 284, 219–227. <https://doi.org/10.1016/j.epsl.2009.04.031>
43
44
45 798 Class, C., Goldstein, S.L., Stute, M., Kurz, M.D., Schlosser, P., 2005. Grand Comore Island:
46 799 A well-constrained “low $^3\text{He}/^4\text{He}$ ” mantle plume. *Earth Planet. Sci. Lett.* 233, 391–409.
47 800 <https://doi.org/10.1016/j.epsl.2005.02.029>
48
49
50
51 801 Claude-Ivanaj, C., Bourdon, B., Allègre, C.J., 1998. Ra–Th–Sr isotope systematics in Grande
52 802 Comore Island: a case study of plume–lithosphere interaction. *Earth Planet. Sci. Lett.*
53 803 164, 99–117. [https://doi.org/10.1016/S0012-821X\(98\)00195-2](https://doi.org/10.1016/S0012-821X(98)00195-2)
54
55
56 804 Coltorti, M., Bonadiman, C., Hinton, R.W., Siena, F., Upton, B.G.J., 1999. Carbonatite
57 805 metasomatism of the oceanic upper mantle: evidence from clinopyroxenes and glasses in
58 806 ultramafic xenoliths of Grande Comore, Indian Ocean. *J. Petrol.* 40, 133–165.
59
60
61
62
63
64
65

- 807 <https://doi.org/10.1016/j.epsl.2014.04.027>
- 1
2 808 Condamine, P., Médard, E., 2014. Experimental melting of phlogopite-bearing mantle at 1
3 809 GPa: Implications for potassic magmatism. *Earth Planet. Sci. Lett.* 397, 80–92.
4
5 810 <https://doi.org/10.1016/j.epsl.2014.04.027>
6
- 7 811 Couch, S., Sparks, R.S.J., Carroll, M.R., 2001. Mineral disequilibrium in lavas explained by
8
9 812 convective self-mixing in open magma chambers. *Nature* 411, 1037–1039.
10
11 813 <https://doi.org/10.1038/35082540>
- 12 814 Courgeon, S., Jorry, S.J., Jouet, G., Camoin, G., BouDagher-Fadel, M.K., Bachèlery, P.,
13
14 815 Caline, B., Boichard, R., Révillon, S., Thomas, Y., 2017. Impact of tectonic and
15
16 816 volcanism on the Neogene evolution of isolated carbonate platforms (SW Indian Ocean).
17
18 817 *Sediment. Geol.* 355, 114–131. <https://doi.org/10.1016/j.sedgeo.2017.04.008>
19
- 20 818 Daly, R.A., 1925. The geology of Ascension island, in: *Proceedings of the American*
21
22 819 *Academy of Arts and Sciences.* JSTOR, pp. 3–80.
- 23 820 Darnet, M., Wawrzyniak, P., Tarits, P., Hautot, S., D’Eu, J.F., 2020. Mapping the geometry of
24
25 821 volcanic systems with magnetotelluric soundings: Results from a land and marine
26
27 822 magnetotelluric survey performed during the 2018–2019 Mayotte seismovolcanic crisis.
28
29 823 *J. Volcanol. Geotherm. Res.* 406, 107046.
30
31 824 <https://doi.org/10.1016/j.jvolgeores.2020.107046>
32
- 33 825 Dautria, J.M., Girod, M., Rahaman, O., 1983. The upper mantle beneath eastern Nigeria:
34
35 826 inferences from ultramafic xenoliths in Jos and Biu volcanics. *J. African Earth Sci.* 1,
36
37 827 331–338.
- 38 828 Debeuf, D., 2004. *Étude de l’évolution volcano-structurale et magmatique de Mayotte*
39
40 829 *(archipel des Comores, océan Indien).* Université de la Reunion.
- 41
42 830 Deniel, C., 1998a. Geochemical and isotopic (Sr, Nd, Pb) evidence for plume–lithosphere
43
44 831 interactions in the genesis of Grande Comore magmas (Indian Ocean). *Chem. Geol.* 144,
45
46 832 281–303. [https://doi.org/10.1016/S0009-2541\(97\)00139-3](https://doi.org/10.1016/S0009-2541(97)00139-3)
- 47 833 Deniel, C., 1998b. Geochemical and isotopic (Sr, Nd, Pb) evidence for plume–lithosphere
48
49 834 interactions in the genesis of Grande Comore magmas (Indian Ocean). *Chem. Geol.* 144,
50
51 835 281–303. [https://doi.org/10.1016/S0009-2541\(97\)00139-3](https://doi.org/10.1016/S0009-2541(97)00139-3)
52
- 53 836 Dofal, A., Fontaine, F.R., Michon, L., Barruol, G., Tkalcic, H., 2018. Crustal structure
54
55 837 variation across the southwestern Indian Ocean from receiver functions determined at
56
57 838 Ocean-Bottom Seismometers, in: *AGU Fall Meeting 2018.* AGU.
- 58 839 Dziewonski, A.M., Chou, T., Woodhouse, J.H., 1981. Determination of earthquake source
59
60 840 parameters from waveform data for studies of global and regional seismicity. *J.*

- 841 Geophys. Res. Solid Earth 86, 2825–2852.
- 1
2 842 Ekström, G., Nettles, M., Dziewoński, A.M., 2012. The global CMT project 2004–2010:
3 843 Centroid-moment tensors for 13,017 earthquakes. *Phys. Earth Planet. Inter.* 200, 1–9.
- 4
5 844 Emerick, C.M., Duncan, R.A., 1982. Age progressive volcanism in the Comores Archipelago,
6
7 845 western Indian Ocean and implications for Somali plate tectonics. *Earth Planet. Sci. Lett.*
8
9 846 60, 415–428. [https://doi.org/10.1016/0012-821X\(82\)90077-2](https://doi.org/10.1016/0012-821X(82)90077-2)
- 10
11 847 Famin, V., Michon, L., Bourhane, A., 2020. The Comoros archipelago: a right-lateral
12
13 848 transform boundary between the Somalia and Lwandle plates. *Tectonophysics* 789,
14
15 849 228539. <https://doi.org/10.1016/j.tecto.2020.228539>
- 16 850 Feuillet, N., 2019. MAYOBS1 cruise, RV Marion Dufresne.
17
18 851 <https://doi.org/10.17600/18001217>
- 19
20 852 Feuillet, N., Jorry, S., Rinnert, E., Thinon, I., Fouquet, Y., 2019. MAYOBS cruises, RV
21
22 853 Marion Dufresne. <https://doi.org/10.18142/291>
- 23
24 854 Feuillet, N., Jorry, S.J., Crawford, W., Deplus, C., Thinon, I., Jacques, E., Saurel, J.M.,
25
26 855 Lemoine, A., Paquet, F., Satriano, C., Aiken, C., Foix, O., Kowalski, P., Laurent, A.,
27
28 856 Rinnert, E., Cathalot, C., Donval, J.P., Guyader, V., Gaillot, A., Scalabrin, C., Moreira,
29
30 857 M., PelRer, A., Beauducel, F., Grandin, R., Ballu, V., Daniel, R., Pelleau, P., Gomez, J.,
31
32 858 Besançon, S., Geli, L., Bernard, P., Bachelery, P., Fouquet, Y., BerRl, D., Lemarchand,
33
34 859 A., Woerd, J. Van der, 2021. Birth of a large volcanic edifice through lithosphere-scale
35
36 860 diking offshore Mayotte (Indian Ocean). *EarthArXiv*. <https://doi.org/10.31223/X5B89P>
- 37
38 861 Flower, M.F.J., 1973. Evolution of basaltic and differentiated lavas from Anjouan, Comores
39
40 862 Archipelago. *Contrib. to Mineral. Petrol.* 38, 237–260.
- 41
42 863 Flower, M.F.J., 1972. Petrology of volcanic rocks from Anjouan, Comores Archipelago. *Bull.*
43
44 864 *Volcanol.* 36, 238–250.
- 45
46 865 Fouquet, Y., Feuillet, N., 2019. MAYOBS4 cruise, RV Marion Dufresne.
47
48 866 <https://doi.org/10.17600/18001238>
- 49
50 867 Fujimaki, H., 1986. Partition coefficients of Hf, Zr, and REE between zircon, apatite, and
51
52 868 liquid. *Contrib. to Mineral. Petrol.* 94, 42–45.
- 53
54 869 Ghiorso, M.S., Gualda, G.A.R., 2015. An H₂O–CO₂ mixed fluid saturation model
55
56 870 compatible with rhyolite-MELTS. *Contrib. to Mineral. Petrol.* 169, 1–30.
57
58 871 <https://doi.org/10.1007/s00410-015-1141-8>
- 59
60 872 Ghiorso, M.S., Sack, R.O., 1995. Chemical mass transfer in magmatic processes IV. A
61
62 873 revised and internally consistent thermodynamic model for the interpolation and
63
64 874 extrapolation of liquid-solid equilibria in magmatic systems at elevated temperatures and
65

- 875 pressures. *Contrib. to Mineral. Petrol.* 119, 197–212.
1
2 876 <https://doi.org/10.1007/BF00307281>
- 3 877 Giehl, C., Marks, M., Nowak, M., 2013. Phase relations and liquid lines of descent of an iron-
4
5 878 rich peralkaline phonolitic melt: an experimental study. *Contrib. to Mineral. Petrol.* 165,
6
7 879 283–304.
- 8
9 880 Grant, T.B., Milke, R., Pandey, S., Jahnke, H., 2013. The Heldburg Phonolite, Central
10
11 881 Germany: Reactions between phonolite and xenocrysts from the upper mantle and lower
12
13 882 crust. *Lithos* 182, 86–101. <https://doi.org/10.1016/j.lithos.2013.09.012>
- 14 883 Grove, T.L., Donnelly-Nolan, J.M., 1986. The evolution of young silicic lavas at Medicine
15
16 884 Lake Volcano, California: Implications for the origin of compositional gaps in calc-
17
18 885 alkaline series lavas. *Contrib. to Mineral. Petrol.* 92, 281–302.
19
20 886 <https://doi.org/10.1007/BF00572157>
- 21
22 887 Gualda, G.A.R., Ghiorso, M.S., Lemons, R. V, Carley, T.L., 2012. Rhyolite-MELTS: a
23
24 888 modified calibration of MELTS optimized for silica-rich, fluid-bearing magmatic
25
26 889 systems. *J. Petrol.* 53, 875–890. <https://doi.org/10.1093/petrology/egr080>
- 27 890 Hajash, A., Armstrong, R.L., 1972. Paleomagnetic and radiometric evidence for the age of the
28
29 891 Comores Islands, west central Indian Ocean. *Earth Planet. Sci. Lett.* 16, 231–236.
30
31 892 [https://doi.org/10.1016/0012-821X\(72\)90195-1](https://doi.org/10.1016/0012-821X(72)90195-1)
- 32
33 893 Irving, A.J., Price, R.C., 1981. Geochemistry and evolution of Iherzolite-bearing phonolitic
34
35 894 lavas from Nigeria, Australia, East Germany and New Zealand. *Geochim. Cosmochim.*
36
37 895 *Acta* 45, 1309–1320. [https://doi.org/10.1016/0016-7037\(81\)90224-6](https://doi.org/10.1016/0016-7037(81)90224-6)
- 38 896 Jochum, K.P., Weis, U., Schwager, B., Stoll, B., Wilson, S.A., Haug, G.H., Andreae, M.O.,
39
40 897 Enzweiler, J., 2016. Reference values following ISO guidelines for frequently requested
41
42 898 rock reference materials. *Geostand. Geoanalytical Res.* 40, 333–350.
43
44 899 <https://doi.org/10.1111/j.1751-908X.2015.00392.x>
- 45 900 Jorry, S.J., 2019. MAYOBS2 cruise, RV Marion Dufresne.
46
47 901 <https://doi.org/10.17600/18001222>
- 48
49 902 Klemme, S., Günther, D., Hametner, K., Prowatke, S., Zack, T., 2006. The partitioning of
50
51 903 trace elements between ilmenite, ulvospinel, armalcolite and silicate melts with
52
53 904 implications for the early differentiation of the moon. *Chem. Geol.* 234, 251–263.
54
55 905 <https://doi.org/10.1016/j.chemgeo.2006.05.005>
- 56 906 Kyle, P.R., Moore, J.A., Thirlwall, M.F., 1992. Petrologic evolution of anorthoclase phonolite
57
58 907 lavas at Mount Erebus, Ross Island, Antarctica. *J. Petrol.* 33, 849–875.
59
60 908 <https://doi.org/doi.org/10.1093/petrology/33.4.849>
- 61
62
63
64
65

- 909 Laporte, D., Lambart, S., Schiano, P., Ottolini, L., 2014. Experimental derivation of nepheline
1 910 syenite and phonolite liquids by partial melting of upper mantle peridotites. *Earth Planet.*
2
3 911 *Sci. Lett.* 404, 319–331. <https://doi.org/10.1093/etroj/40.1.133>
4
5 912 Le Bas, M.J., Streckeisen, A.L., 1991. The IUGS systematics of igneous rocks. *J. Geol. Soc.*
6
7 913 London. 148, 825–833.
8
9 914 Le roex, A.P., Cliff, R.A., Adair, B.J.I., 1990. Tristan da Cunha, South Atlantic: geochemistry
10
11 915 and petrogenesis of a basanite-phonolite lava series. *J. Petrol.* 31, 779–812.
12
13 916 <https://doi.org/10.1093/etrology/31.4.779>
14
15 917 Lemoine, A., Briole, P., Bertil, D., Roullé, A., Foumel, M., THINON, I., Raucoules, D.,
16 918 Michele, M. de, Valty, P., 2020. The 2018-2019 seismo-volcanic crisis east of Mayotte,
17
18 919 Comoros islands: seismicity and ground deformation markers of an exceptional
19
20 920 submarine eruption. <https://doi.org/10.31223/osf.io/d46xj>
21
22 921 Loges, A., Schultze, D., Klügel, A., Lucassen, F., 2019. Phonolitic melt production by
23
24 922 carbonatite Mantle metasomatism: evidence from Eger Graben xenoliths. *Contrib. to*
25
26 923 *Mineral. Petrol.* 174, 93. <https://doi.org/10.1007/s00410-019-1630-2>
27
28 924 Ludden, J.N., 1977. The mineral chemistry and origin of xenoliths from the lavas of Anjouan,
29
30 925 Comores Archipelago, western Indian Ocean. *Contrib. to Mineral. Petrol.* 64, 91–107.
31
32 926 Luhr, J.F., Carmichael, I.S.E., Varekamp, J.C., 1984. The 1982 eruptions of El Chichón
33
34 927 Volcano, Chiapas, Mexico: mineralogy and petrology of the anhydrite-bearing pumices.
35
36 928 *J. Volcanol. Geotherm. Res.* 23, 69–108. [https://doi.org/10.1016/0377-0273\(84\)90057-X](https://doi.org/10.1016/0377-0273(84)90057-X)
37
38 929 Mahood, G.A., Stimac, J.A., 1990. Trace-element partitioning in pantellerites and trachytes.
39
40 930 *Geochim. Cosmochim. Acta* 54, 2257–2276. [https://doi.org/10.1016/0016-](https://doi.org/10.1016/0016-7037(90)90050-U)
41
42 931 [7037\(90\)90050-U](https://doi.org/10.1016/0016-7037(90)90050-U)
43
44 932 Marks, M., Markl, G., 2003. Ilímaussaq ‘en miniature’: closed-system fractionation in an
45
46 933 agpaitic dyke rock from the Gardar Province, South Greenland (contribution to the
47
48 934 mineralogy of Ilímaussaq no. 117). *Mineral. Mag.* 67, 893–919.
49
50 935 <https://doi.org/10.1180/0026461036750150>
51
52 936 Matsui, Y., Onuma, N., Nagasawa, H., Higuchi, H., Banno, S., 1977. Crystal structure control
53
54 937 in trace element partition between crystal and magma. *Bull. Minéralogie* 100, 315–324.
55
56 938 McDonough, W.F., Sun, S.-S., 1995. The composition of the Earth. *Chem. Geol.* 120, 223–
57
58 939 253. [https://doi.org/https://doi.org/10.1016/0009-2541\(94\)00140-4](https://doi.org/https://doi.org/10.1016/0009-2541(94)00140-4)
59
60 940 Michon, L., 2016. The volcanism of the Comoros archipelago integrated at a regional scale,
61
62 941 in: *Active Volcanoes of the Southwest Indian Ocean*. Springer, pp. 333–344.
63
64 942 https://doi.org/10.1007/978-3-642-31395-0_21
65

- 943 Moussallam, Y., Oppenheimer, C., Scaillet, B., Kyle, P.R., 2013. Experimental phase-
1 944 equilibrium constraints on the phonolite magmatic system of Erebus Volcano,
2 945 Antarctica. *J. Petrol.* 54, 1285–1307. [https://doi.org/10.1093/](https://doi.org/10.1093/petrology/egt012)
3 946 Nash, W.P., Carmichael, I.S.E., Johnson, R.W., 1969. The mineralogy and petrology of
4 947 Mount Suswa, Kenya. *J. Petrol.* 10, 409–439.
5 948 Neave, D.A., Maclennan, J., Thordarson, T., Hartley, M.E., 2015. The evolution and storage
6 949 of primitive melts in the Eastern Volcanic Zone of Iceland: the 10 ka Grímsvötn tephra
7 950 series (ie the Saksunarvatn ash). *Contrib. to Mineral. Petrol.* 170, 21.
8 951 <https://doi.org/10.1007/s00410-015-1170-3>
9 952 Nehlig, P., Lacquement, F., Bernard, J., Caroff, M., Deparis, J., Jaouen, T., Pelleter, A.A.,
10 953 Perrin, J., Prognon, C., Vittecoq, B., 2013. Notice de la carte géologique de Mayotte.
11 954 BRGM/RP-61803-FR, 135 p., 45 ill., 1 ann.
12 955 Nougier, J., Cantagrel, J.M., Karche, J.P., 1986. The Comores archipelago in the western
13 956 Indian Ocean: volcanology, geochronology and geodynamic setting. *J. African Earth Sci.*
14 957 5, 135–144. [https://doi.org/10.1016/0899-5362\(86\)90003-5](https://doi.org/10.1016/0899-5362(86)90003-5)
15 958 Pelleter, A.-A., Caroff, M., Cordier, C., Bachèlery, P., Nehlig, P., Debeuf, D., Arnaud, N.,
16 959 2014. Melilite-bearing lavas in Mayotte (France): An insight into the mantle source
17 960 below the Comores. *Lithos* 208, 281–297. <https://doi.org/10.1016/j.lithos.2014.09.012>
18 961 Price, R.C., Green, D.H., 1972. Lherzolite nodules in a “mafic phonolite” from north-east
19 962 Otago, New Zealand. *Nat. Phys. Sci.* 235, 133–134.
20 963 <https://doi.org/10.1038/physci235133a0>
21 964 Prowatke, S., Klemme, S., 2006. Trace element partitioning between apatite and silicate
22 965 melts. *Geochim. Cosmochim. Acta* 70, 4513–4527.
23 966 Putirka, K.D., 2008. Thermometers and Barometers for Volcanic Systems. *Rev. Mineral.*
24 967 *Geochemistry* 69, 61–120. <https://doi.org/10.2138/rmg.2008.69.3>
25 968 Reubi, O., Blundy, J., 2009. A dearth of intermediate melts at subduction zone volcanoes and
26 969 the petrogenesis of arc andesites. *Nature* 461, 1269–1273.
27 970 <https://doi.org/10.1038/nature08510>
28 971 ReVoSiMa, 2021. Bulletin n°21 de l’activité sismo-volcanique à Mayotte, du 1 au 31 janvier
29 972 2021. <https://doi.org/ISSN:2680-1205>
30 973 Romano, P., Scaillet, B., White, J.C., Andújar, J., Di Carlo, I., Rotolo, S.G., 2020.
31 974 Experimental and thermodynamic constraints on mineral equilibrium in pantelleritic
32 975 magmas. *Lithos* 376, 105793. <https://doi.org/10.1016/j.lithos.2020.105793>
33 976 Rutherford, M.J., 1969. An experimental determination of iron biotite-alkali feldspar
34
35
36
37
38
39
40
41
42
43
44
45
46
47
48
49
50
51
52
53
54
55
56
57
58
59
60
61
62
63
64
65

- 977 equilibria. *J. Petrol.* 10, 381–408.
- 1
2 978 Scaillet, B., Pichavant, M., Cioni, R., 2008. Upward migration of Vesuvius magma chamber
3
4 979 over the past 20,000 years. *Nature* 455, 216–219. <https://doi.org/10.1038/nature07232>
- 5 980 Schiano, P., Bourdon, B., Clocchiatti, R., Massare, D., Varela, M.E., Bottinga, Y., 1998.
6
7 981 Low-degree partial melting trends recorded in upper mantle minerals. *Earth Planet. Sci.*
8
9 982 *Lett.* 160, 537–550. [https://doi.org/10.1016/S0012-821X\(98\)00109-5](https://doi.org/10.1016/S0012-821X(98)00109-5)
- 10
11 983 Schnetzler, C.C., Philpotts, J.A., 1970. Partition coefficients of rare-earth elements between
12
13 984 igneous matrix material and rock-forming mineral phenocrysts—II. *Geochim.*
14
15 985 *Cosmochim. Acta* 34, 331–340. [https://doi.org/10.1016/0016-7037\(70\)90110-9](https://doi.org/10.1016/0016-7037(70)90110-9)
- 16 986 Späth, A., Roex, A.P. Le, Duncan, R.A., 1996. The geochemistry of lavas from the Comores
17
18 987 Archipelago, Western Indian Ocean: petrogenesis and mantle source region
19
20 988 characteristics. *J. Petrol.* 37, 961–991. <https://doi.org/10.1093/petrology/37.4.961>
- 21
22 989 Stamps, D.S., Kreemer, C., Fernandes, R., Rajaonarison, T.A., Rambolamanana, G., 2021.
23
24 990 Redefining East African Rift System kinematics. *Geology*.
- 25 991 Stix, J., Gorton, M.P., 1990. Variations in trace element partition coefficients in sanidine in
26
27 992 the Cerro Toledo Rhyolite, Jemez Mountains, New Mexico: Effects of composition,
28
29 993 temperature, and volatiles. *Geochim. Cosmochim. Acta* 54, 2697–2708.
- 30
31 994 Strong, D.F., 1972. Petrology of the island of Moheli, western Indian Ocean. *Geol. Soc. Am.*
32
33 995 *Bull.* 83, 389–406.
- 34
35 996 Tatsumi, Y., Suzuki, T., 2009. Tholeiitic vs calc-alkalic differentiation and evolution of arc
36
37 997 crust: constraints from melting experiments on a basalt from the Izu–Bonin–Mariana
38
39 998 Arc. *J. Petrol.* 50, 1575–1603. <https://doi.org/10.1093/petrology/egp044>
- 40 999 Thompson, R.N., Flower, M.F.J., 1971. One-atmosphere melting and crystallization relations
41
42 1000 of lavas from Anjouan, Comores Archipelago, Western Indian Ocean. *Earth Planet. Sci.*
43
44 1001 *Lett.* 12, 97–107. [https://doi.org/10.1016/0012-821X\(71\)90060-4](https://doi.org/10.1016/0012-821X(71)90060-4)
- 45 1002 Tzevahirtzian, A., Zaragosi, S., Bachelery, P., Biscara, L., Marchès, E., 2021. Submarine
46
47 1003 morphology of the Comoros volcanic archipelago. *Mar. Geol.* 432.
48
49 1004 <https://doi.org/10.1016/j.margeo.2020.106383>
- 50
51 1005 Ubide, T., Mollo, S., Zhao, J., Nazzari, M., Scarlato, P., 2019. Sector-zoned clinopyroxene as
52
53 1006 a recorder of magma history, eruption triggers, and ascent rates. *Geochim. Cosmochim.*
54
55 1007 *Acta* 251, 265–283. <https://doi.org/10.1016/j.gca.2019.02.021>
- 56
57 1008 Zinke, J., Reijmer, J.J.G., Thomassin, B.A., Dullo, W.-C., Grootes, P.M., Erlenkeuser, H.,
58
59 1009 2003. Postglacial flooding history of Mayotte lagoon (Comoro archipelago, southwest
60 1010 Indian Ocean). *Mar. Geol.* 194, 181–196. [https://doi.org/10.1016/S0025-3227\(02\)00705-](https://doi.org/10.1016/S0025-3227(02)00705-)
- 61
62
63
64
65

1011 3

1
2 1012

3
4 1013 **Figure Captions:**

5
6 1014

7 1015 **Fig. 1:** a) Location of Comoros archipelago in the Mozambique Channel. b) Geological map
8
9 1016 of the active submarine volcanic ridge showing the location of our samples offshore and on
10
11 1017 land. Ages are from (Debeuf, 2004; Emerick and Duncan, 1982; Hajash and Armstrong,
12
13 1018 1972; Nougier et al., 1986; Pelleter et al., 2014). DR labels correspond to the dredged
14
15 1019 samples.

16
17 1020

18 1021 **Fig. 2:** Geochemical signature of the volcanic ridge east of Mayotte. a) Classification of our
19
20 1022 samples using the TAS diagram after Le bas and Streckeis, (1991), b) FeO vs MgO
21
22 1023 diagram, c) CaO vs MgO diagram, d) Al₂O₃ vs MgO diagram. Blue arrows and green arrows
23
24 1024 respectively show the moderately silica-undersaturated (Karthala-type) and the highly silica-
25
26 1025 undersaturated (La Grille-type) trends for Mayotte lavas (from Bachèlery & Hémond 2016).

27
28 1026

29 1027 **Fig. 3:** Trace element variations in basanites and phonolites samples. a) Chondrite-
30
31 1028 normalized REE patterns, b) Spider diagrams of incompatible trace elements normalized to
32
33 1029 primitive-mantle concentrations (McDonough and Sun, 1995), c) V vs Th diagram, d) Co vs
34
35 1030 MgO diagram, e) Sc vs MgO diagram and f) Ba vs SiO₂ diagram.

36
37 1031

38 1032 **Fig. 4:** Textural and petrological features of basanite lavas sampled offshore on the submarine
39
40 1033 volcanic ridge (a) MAY02-DR060201m and b) MAY04-DR090104), and c) on Petite Terre
41
42 1034 Island (MAY181214-12). Mantle xenoliths in phonolites lavas: d) MAY02-DR070208E, e)
43
44 1035 MAY181215-14a, f) MAY190911-6a) contain large olivine and orthopyroxene crystals and
45
46 1036 smaller clinopyroxene and spinel crystals.

47
48 1037

49 1038 **Fig. 5:** Textural and petrological features of phonolite lavas sampled offshore on the active
50
51 1039 submarine volcanic ridge a) MAY02-DR0701v, b) MAY02-DR060204, c) MAY01-DR0202,
52
53 1040 and d) on Petite Terre Island (MAY181215-14b). Phonolites have a trachytic texture with
54
55 1041 laths of alkali feldspar (Afs), and skeletal to subhedral olivine (Fa) microphenocrysts
56
57 1042 intergrown with apatite (Ap) and oxide (Ox).

58
59 1043

60
61
62
63
64
65

Fig. 6: Mineral compositions analyzed in the sampled rocks. a) olivine, b) clinopyroxene and orthopyroxene, c) Fe-Ti oxides, d) feldspar. Our data are compared to minerals in Comoros lavas (Coltorti et al., 1999; Flower, 1972; Ludden, 1977; Schiano et al., 1998; Späth et al., 1996). The two parallel clinopyroxene trends correspond to sector zoning.

Fig. 7: Rhyolite-MELTS models using MAY01-DR0105 basanite as parental magma. Models were run to test if the phonolites can be derived by deep fractional crystallization of the basanites. For each model, temperature decreases from 1200 to 700 °C, with a 10 °C step. We tested a-c) a range of possible pressures from 0.4 to 1.2 GPa, d-f) H₂O concentrations from 1.0 wt% to 5.0 wt%, and g-i) a range of oxygen fugacities buffered at FMQ+1, NNO~FMQ+0.5, FMQ, FMQ-1 and FMQ-2.

Fig. 8: Nature and depth of the source. REE elements could indicate two different sources for basanitic and phonolitic magmas. However, we suggest that REE elements used for this interpretation are impacted by apatite crystallization. b) Model REE patterns obtained by 80% fractional crystallization of a cumulate containing 3-4 wt% apatite (assuming REE are perfectly incompatible in all other phases) compared with phonolite patterns using different partition coefficients (Fujimaki, 1986; Luhr et al., 1984; Mahood and Stimac, 1990; Prowatke and Klemme, 2006).

Fig. 9: Barometric results plotted on a N140 cross section parallel to the volcanic ridge and compared to seismic events (ReVoSiMa, 2021) and magnetotelluric interpretation (presence of melt, Darnet et al., 2020). The latitude and longitude position for each sample is derived from the dredges location. Clinopyroxene barometry from equation 32a of (Putirka, 2008), which has a typical error of 0.28 GPa (9 km). Clinopyroxene/Orthopyroxene barometry in mantle xenoliths from equation (38) of Putirka (2008).

Fig. 10: Cartoon illustrating the magmatic system feeding the active volcanic ridge of Mayotte. The magma formed between 80 – 100 km of depth and then rises until it reaches a deep magma chamber (< 35 km). Using whole-rock geochemistry, Berthod et al., (2021) suggested that the magma have undergone fifty percent of crystallization in this reservoir (twenty percent of olivine and eighty percent of clinopyroxene). Following an internal or external trigger, the eruption begins, and magma rises to the surface. From this stage, we propose three scenarios: In the first scenario the magma rises directly and quickly to the

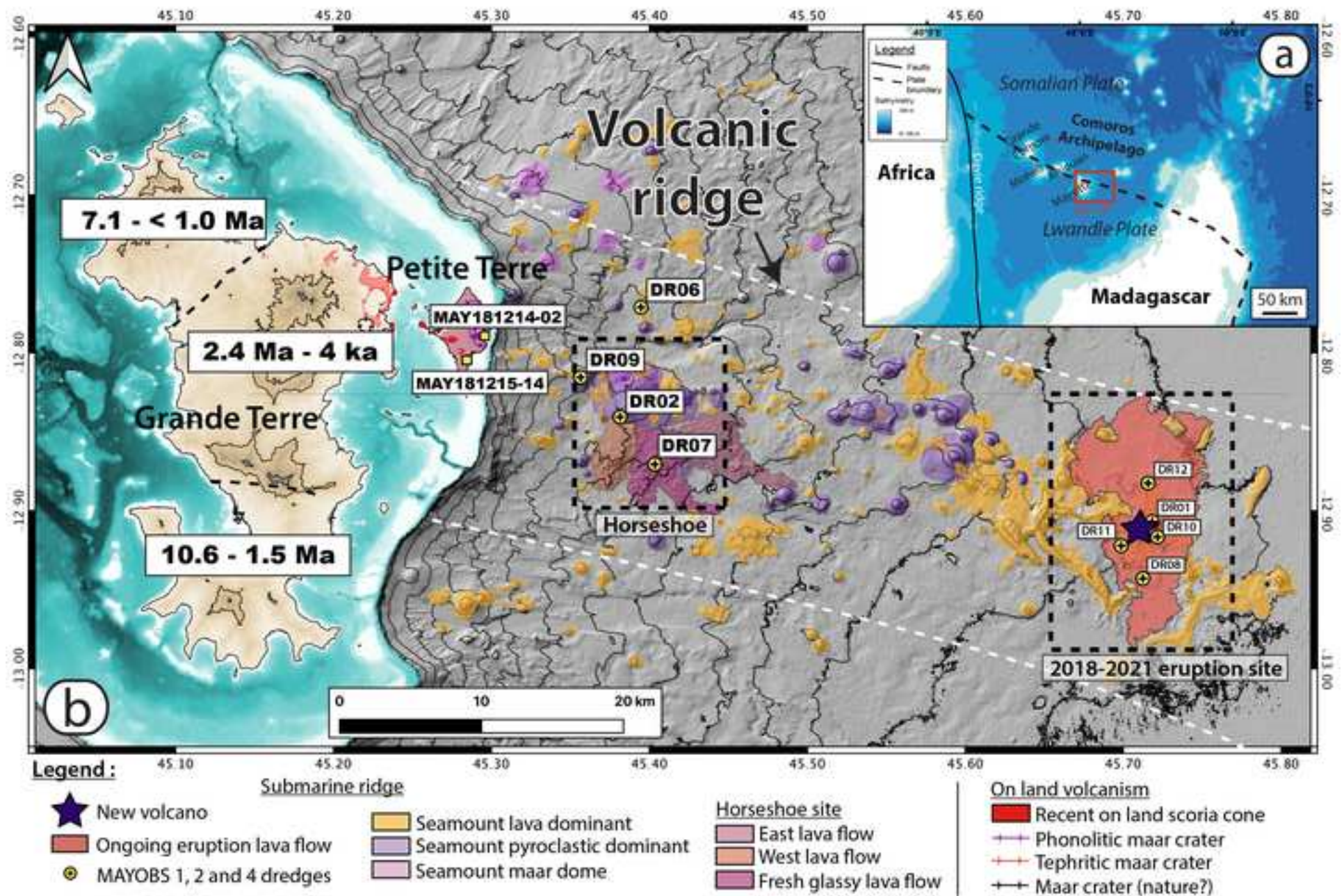
1078 surface generating the aphanitic basanites (Berthod et al., 2021). In the second, the basanitic
1079 magma stalls at the Moho interface before resuming its ascent toward the surface. Finally, in
1080 the last scenario the basanitic magma stops and the depth of the Moho and evolves to
1081 phonolite with 81% of crystallization (anorthoclase (30%), olivine (12.5 %), magnetite (15.5
1082 %), apatite (5 %), ilmenite (4 %) and clinopyroxene (34 %)) in a Moho reservoir. * Dofal et
1083 al., (2018).

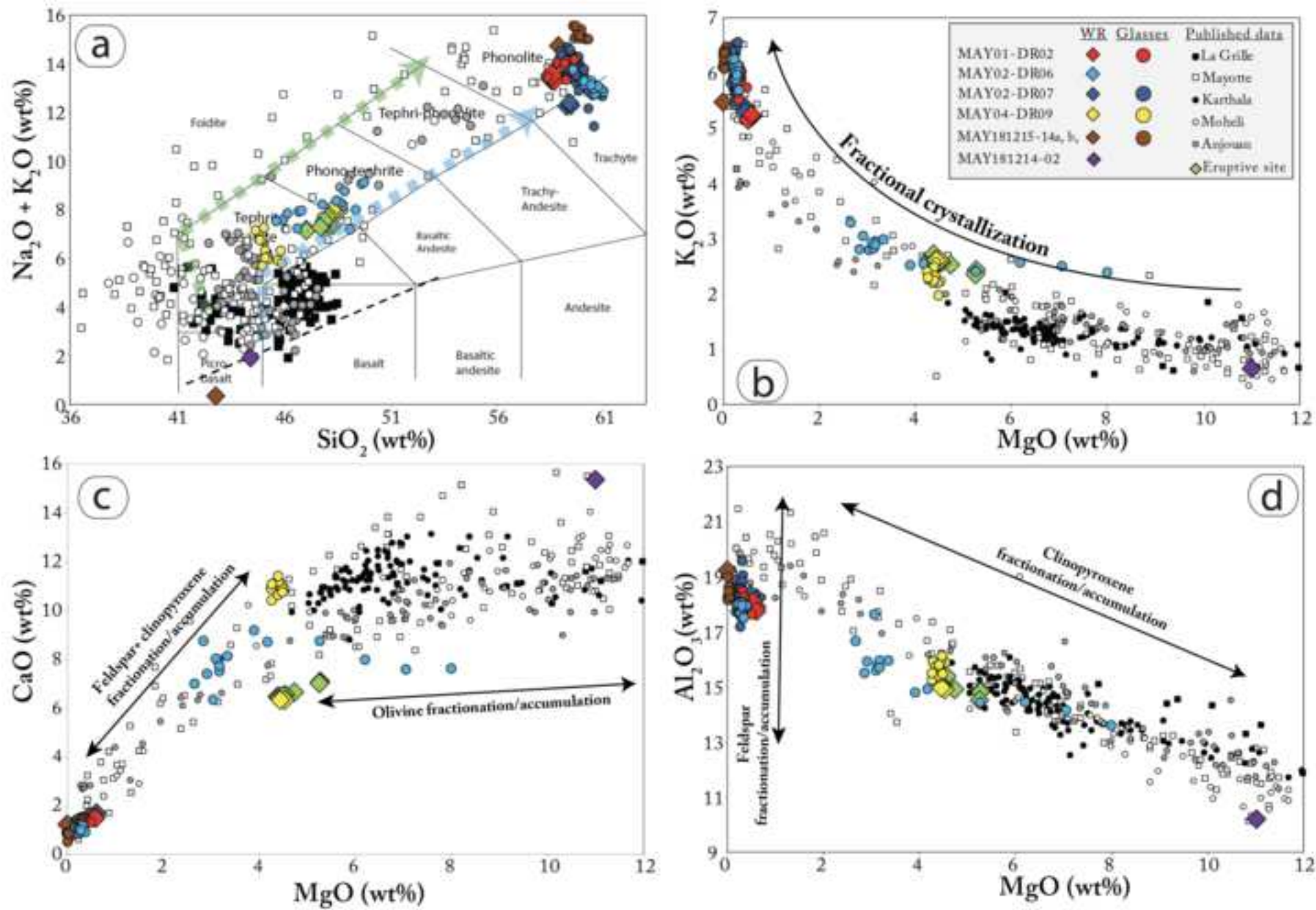
1084
1085

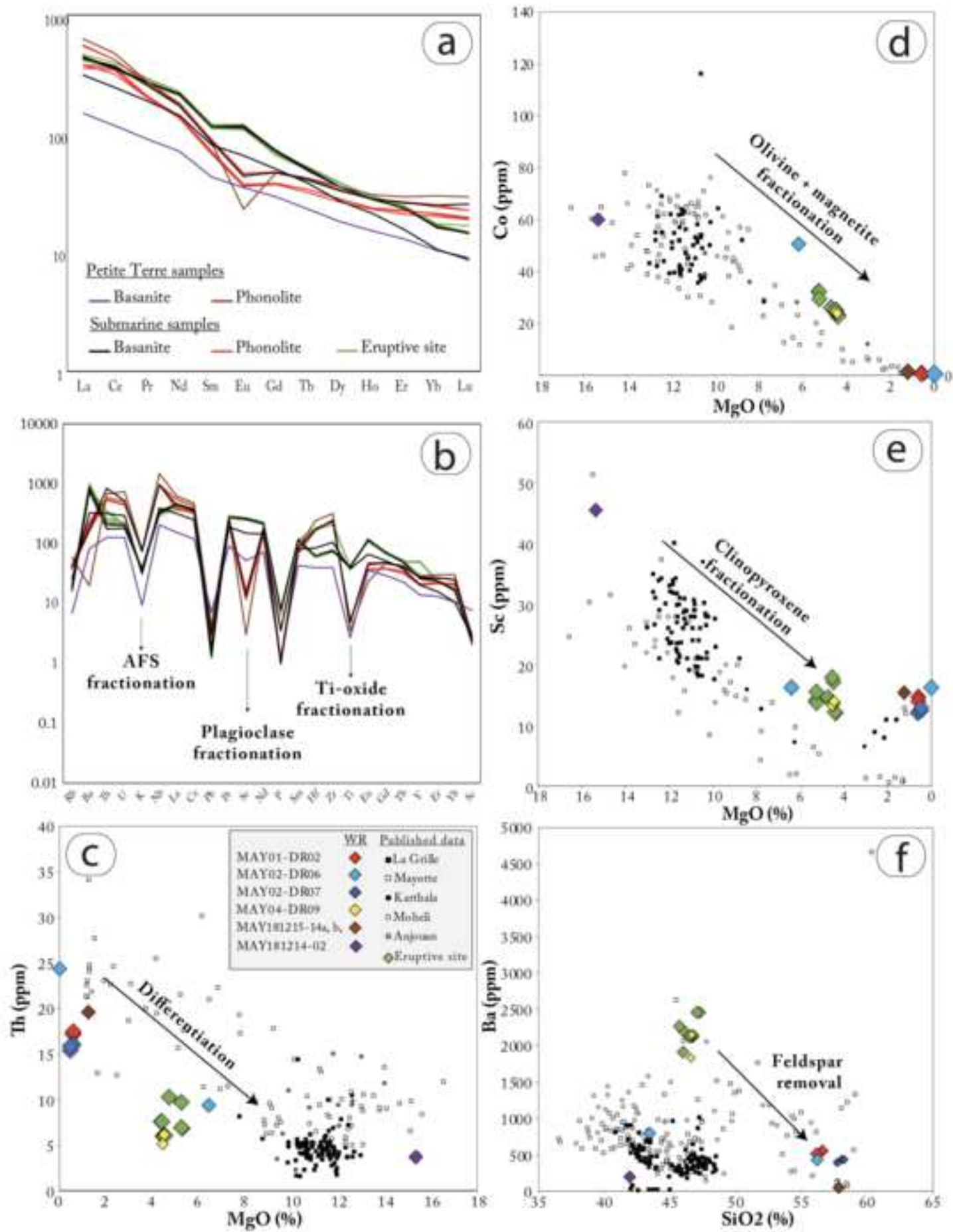
1086 *Table Captions:*

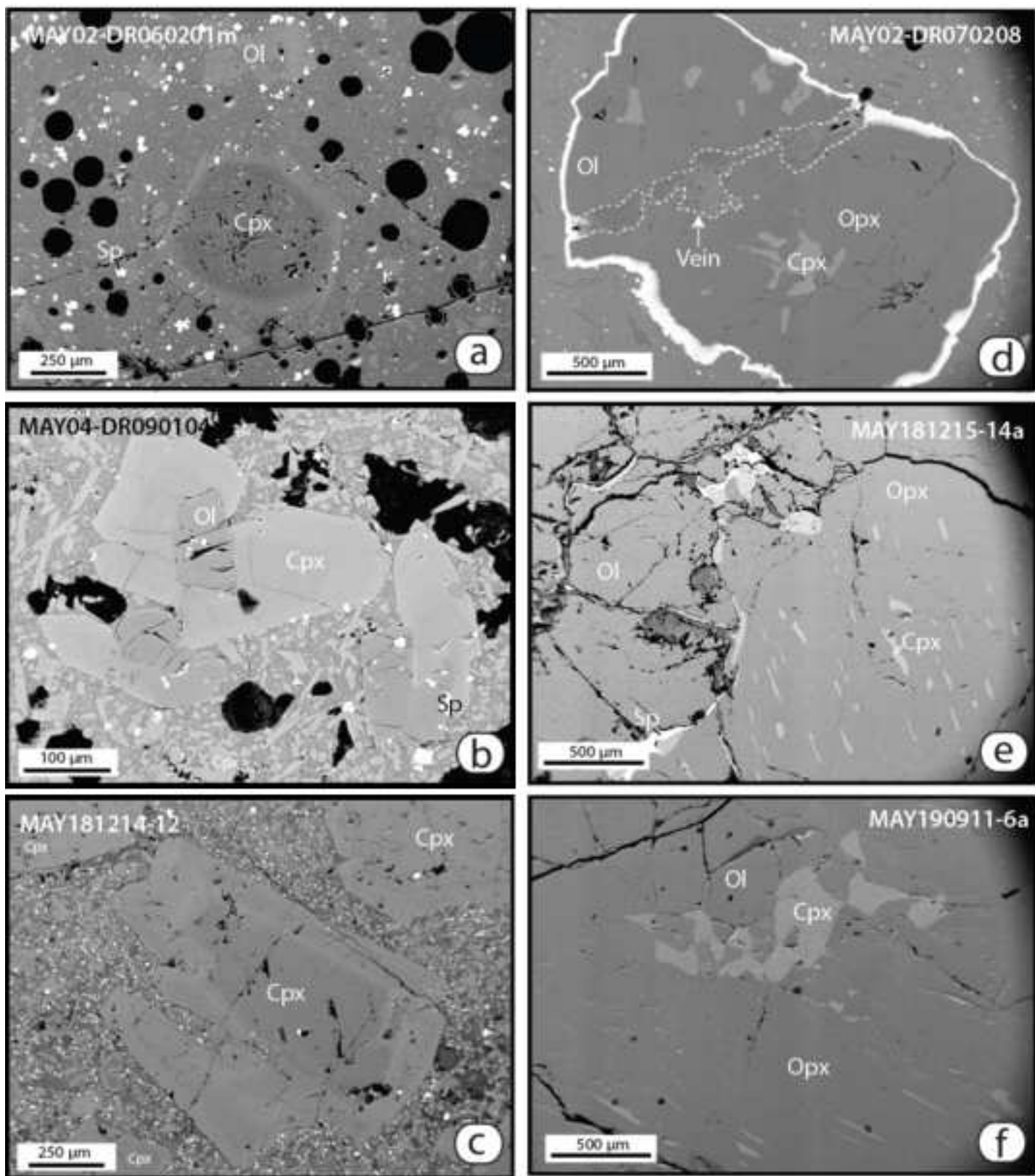
1087
1088 **Tab. 1:** Dredges and on land sample's locations
1089

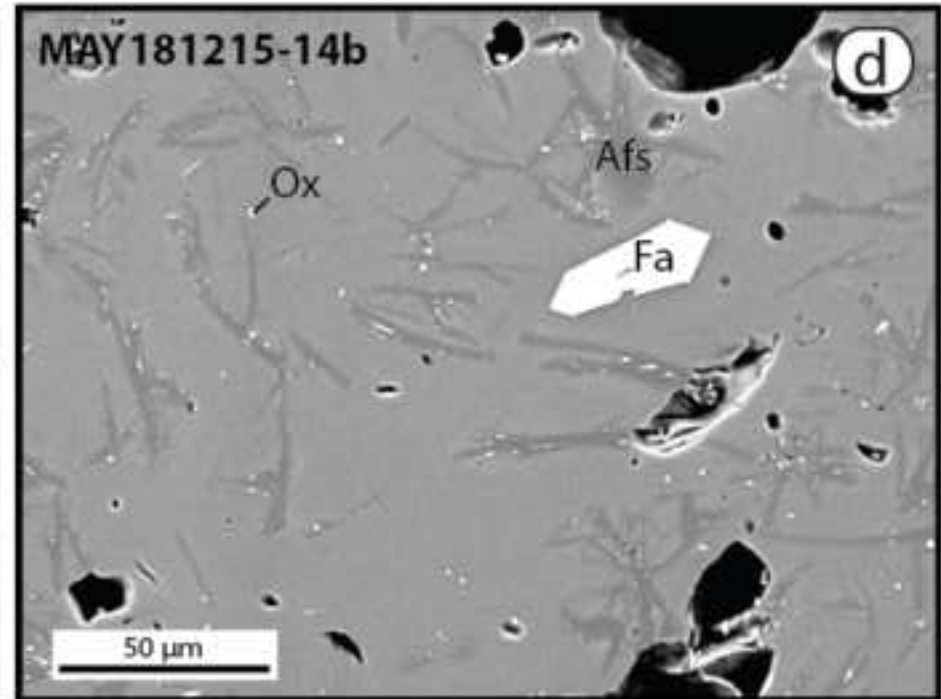
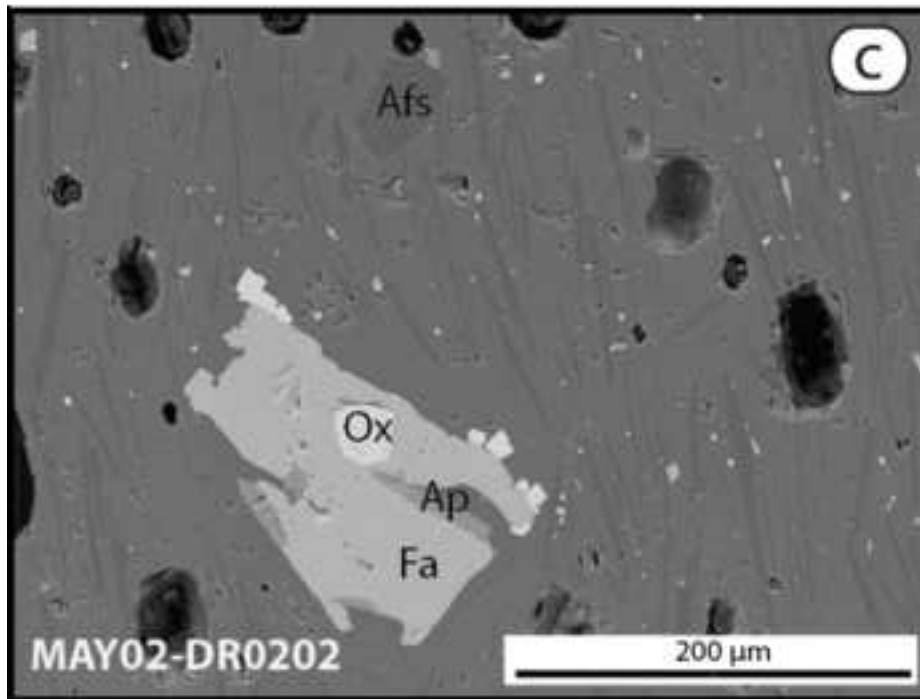
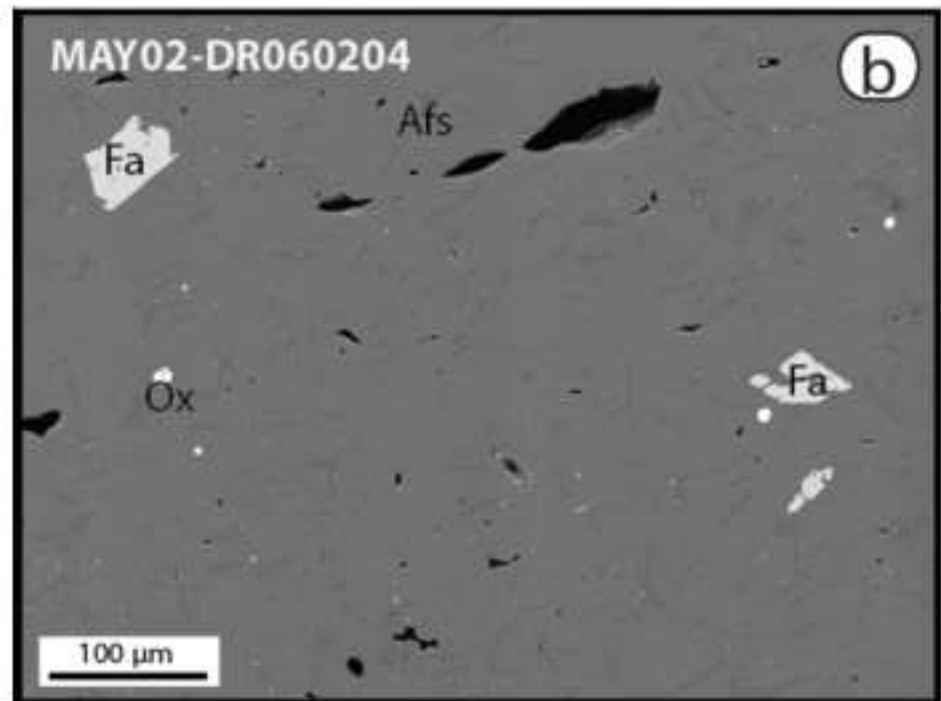
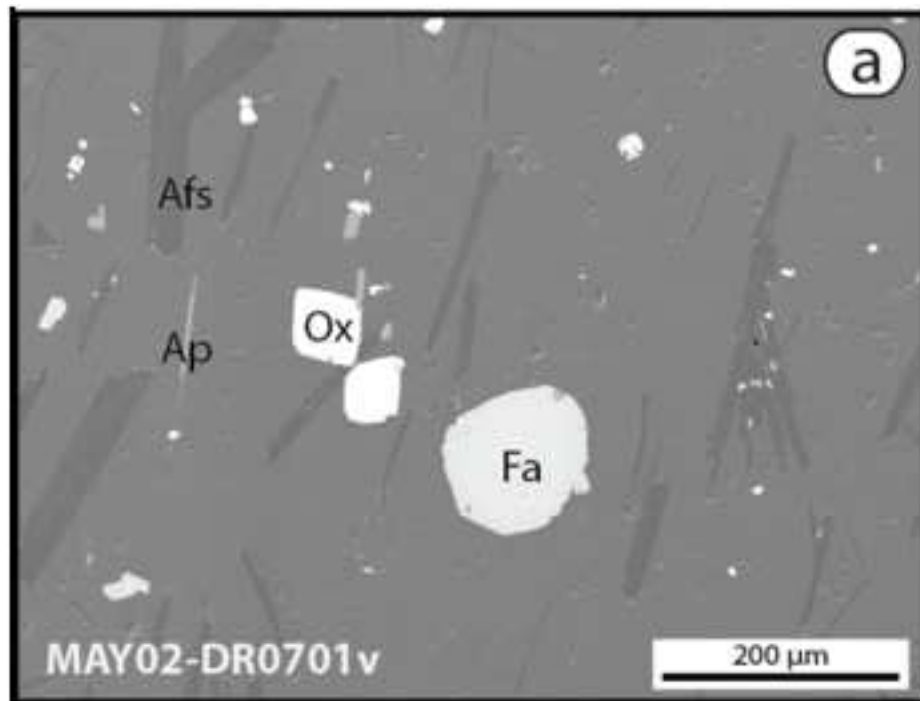
1090
1091
1092
1093
1094
1095
1096
1097
1098
1099
1100
1101
1102
1103
1104
1105
1106
1107
1108
1109
1110
1111
1112
1113
1114
1115
1116
1117
1118
1119
1120
1121
1122
1123
1124
1125
1126
1127
1128
1129
1130
1131
1132
1133
1134
1135
1136
1137
1138
1139
1140
1141
1142
1143
1144
1145
1146
1147
1148
1149
1150
1151
1152
1153
1154
1155
1156
1157
1158
1159
1160
1161
1162
1163
1164
1165











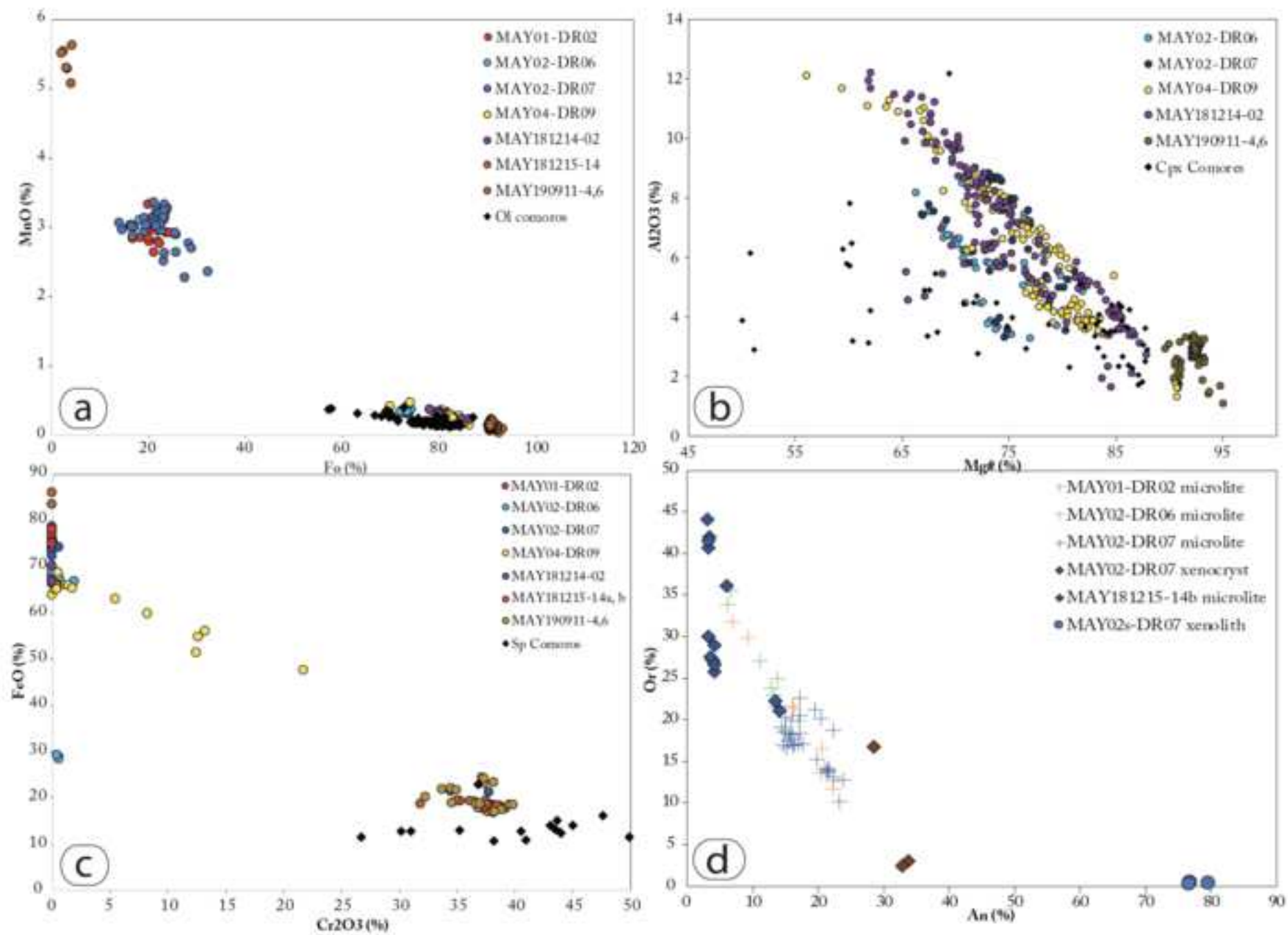
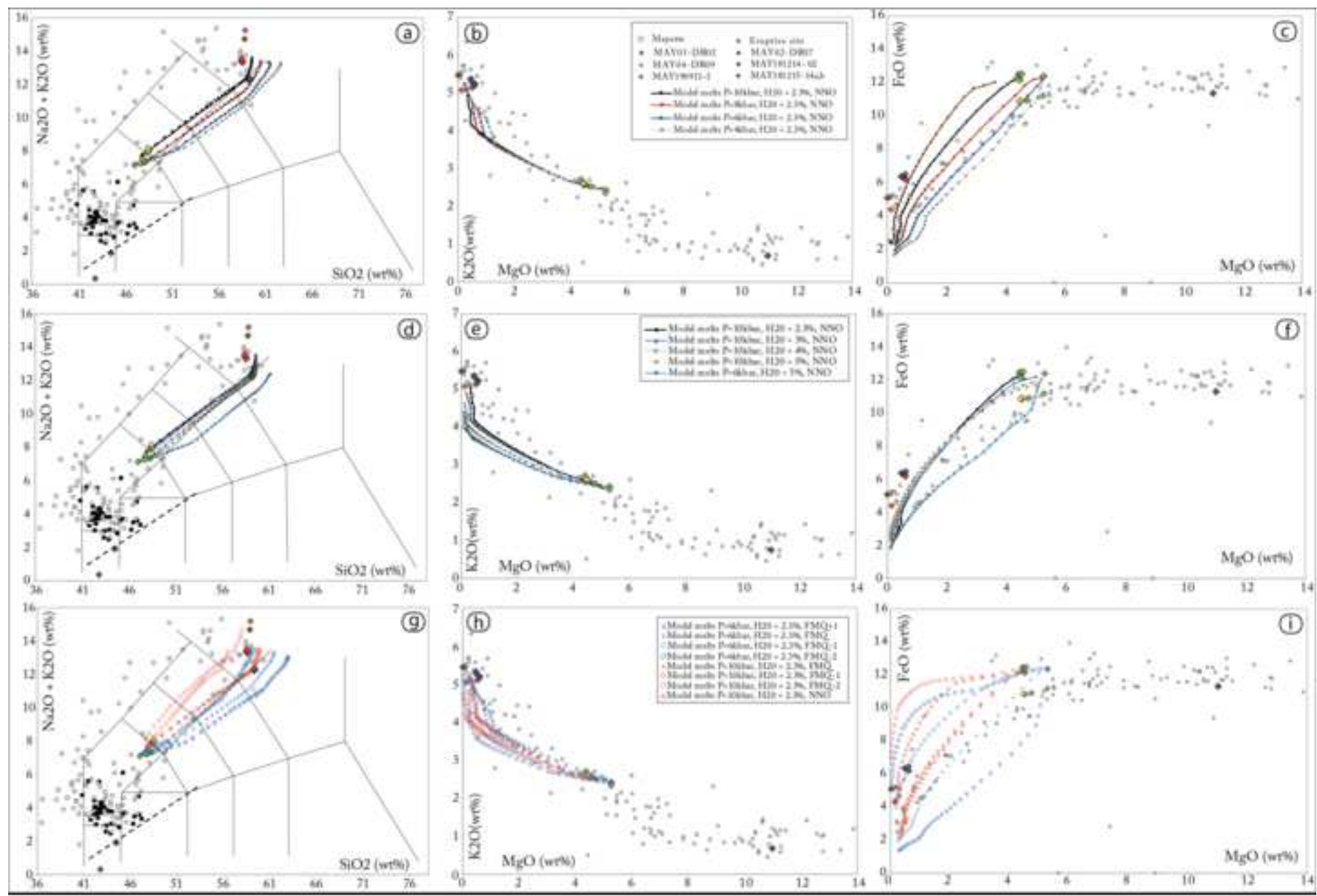
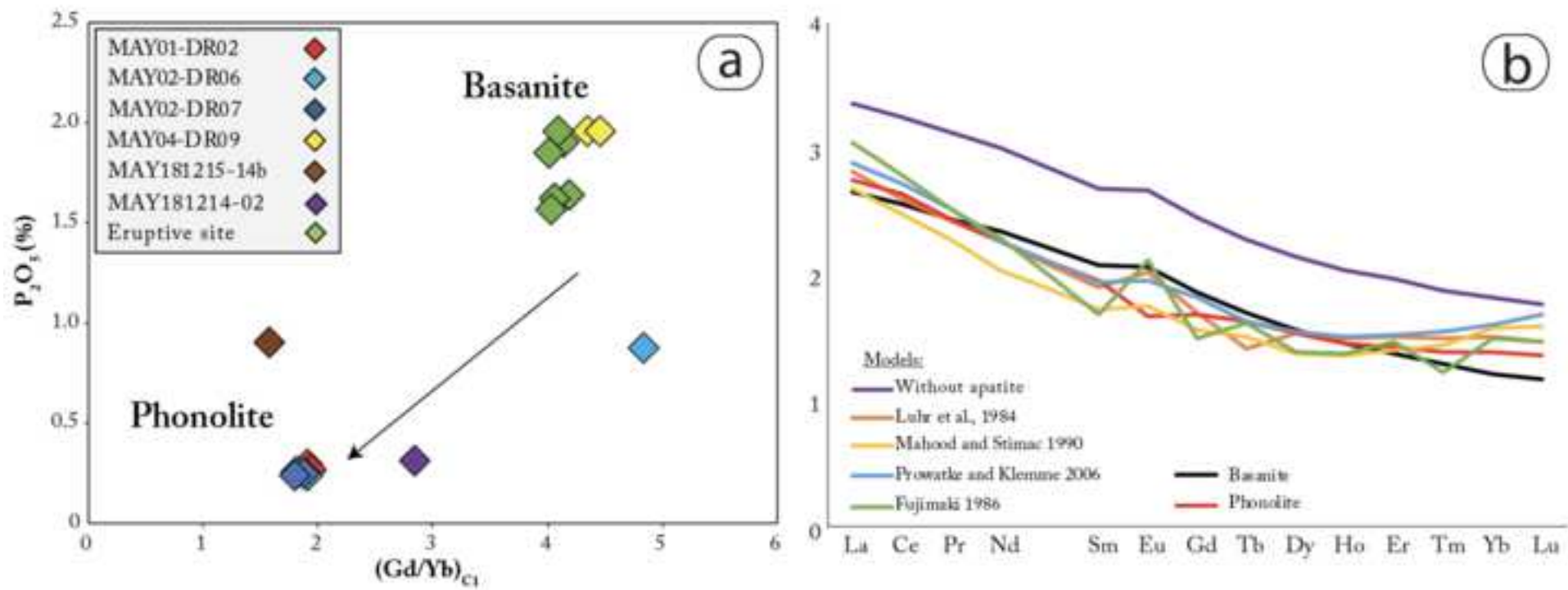
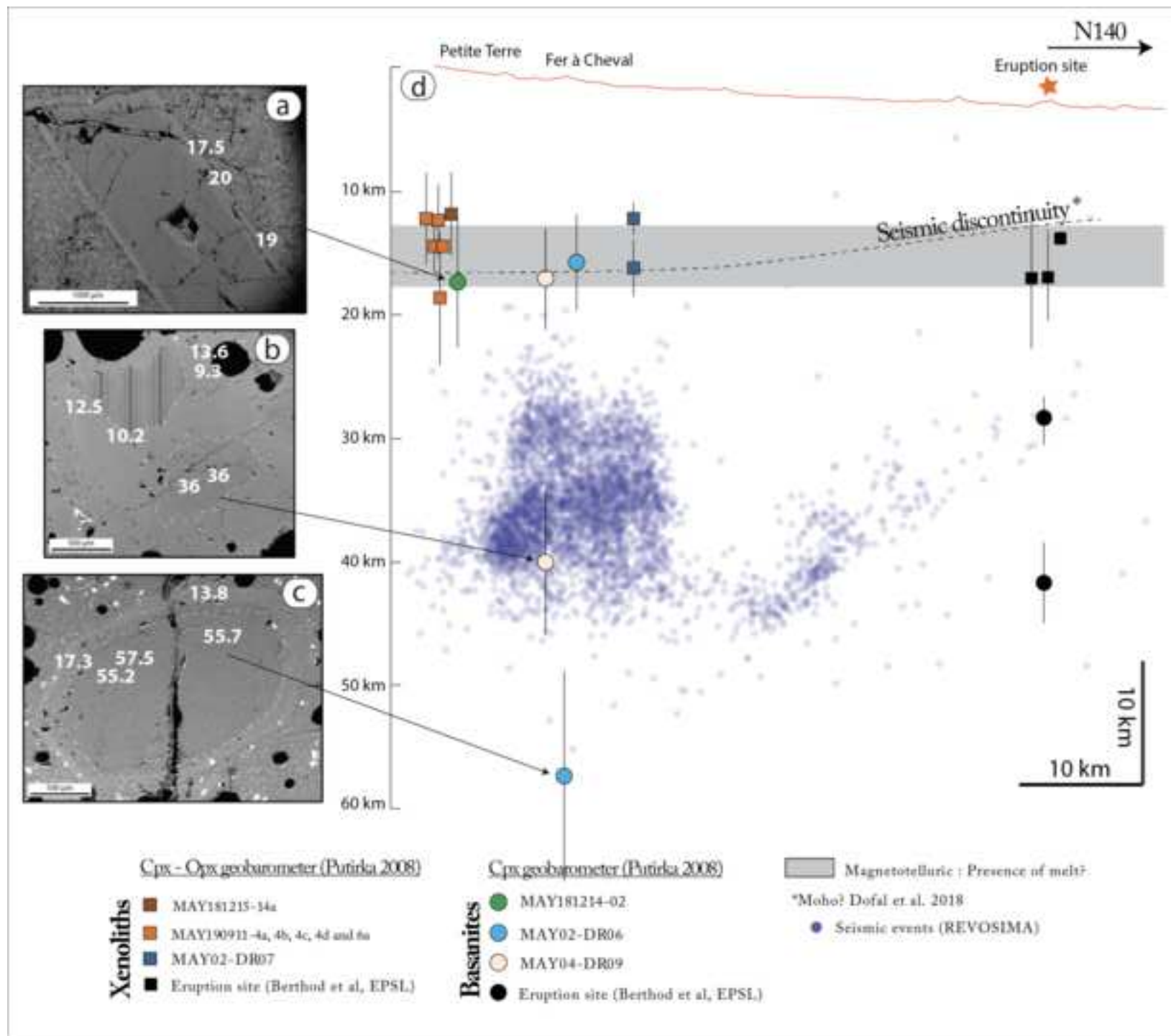
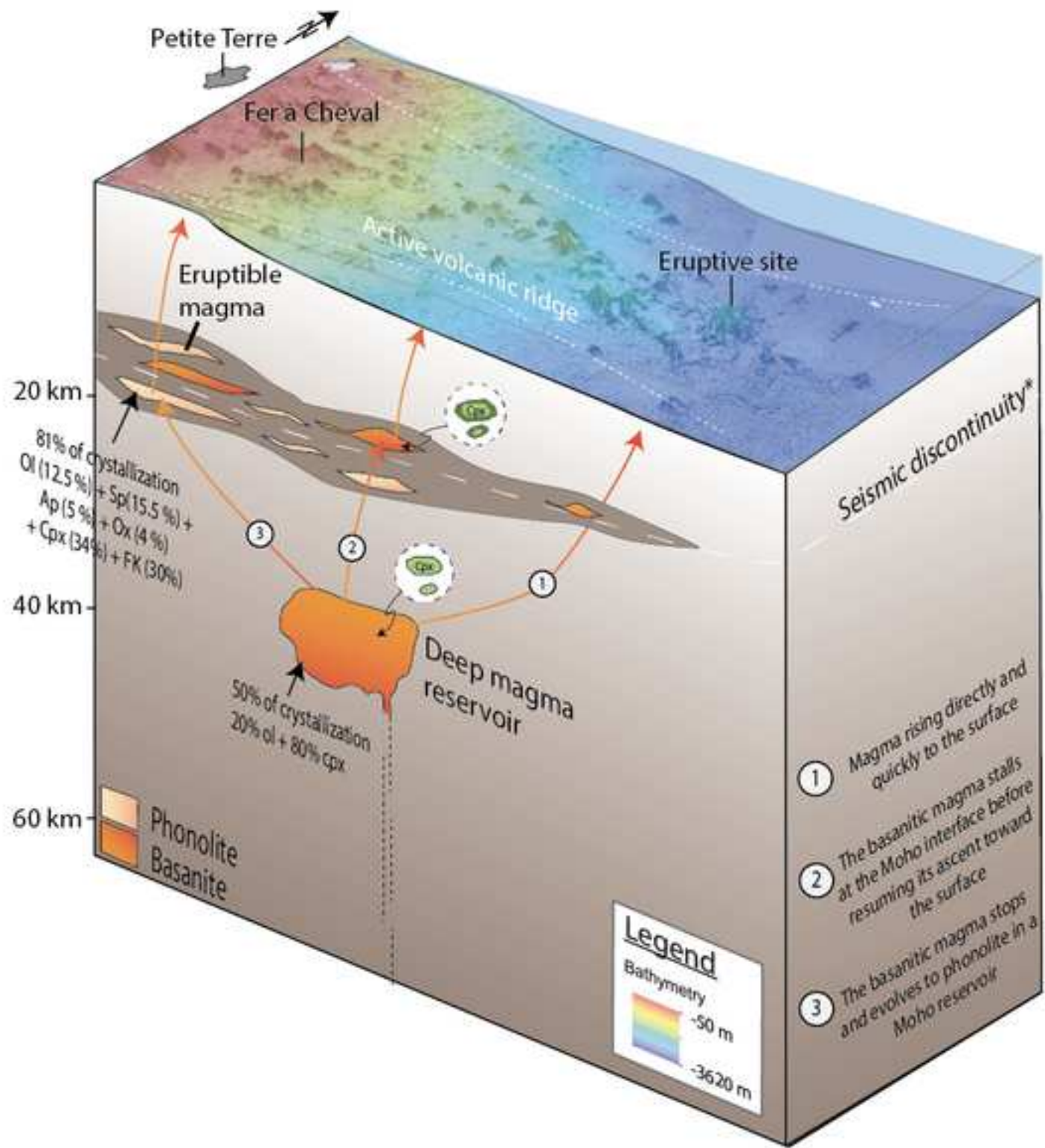


Figure 7









<i>Dredges</i>	<i>Oceanographic cruise</i>	<i>DOI : 10.18142/291</i>
DR02	MAYOBS 1	10.17600/18001217
DR06	MAYOBS 2	10.17600/18001222
DR07	MAYOBS 4	10.17600/18001238
DR09	MAYOBS 4	10.17600/18001238

On land sample		X
MAY181214-02	Petite Terre	45.297496 E
MAY181215-14	Petite Terre	45.286375 E

Start dredging			End dredging		
<i>Latitude</i>	<i>Longitude</i>	<i>Depth</i>	<i>Latitude</i>	<i>Longitude</i>	<i>Depth</i>
12°50,44' S	45°22,89' E	1370 m	12°50,35' S	45°22,94' E	1280 m
12°46.27 S	45°23.86 E	1267 m	12°46.27 S	45°23.48 E	1429 m
12°52.35 S	45°24.46 E	1590 m	12°52.08 S	45°23.96 E	1585 m
12° 48.84' S	45°21.42' E	1125 m	12° 48.99' S	45°21.35' E	945 m

Y
12.783116 S
12.800904 S